Interleukin-1 prevents SARS-CoV-2-induced membrane fusion to restrict viral transmission via induction of actin bundles

Xu Zheng[1,#], Shi Yu[1,#,$], Yanqiu Zhou[2,#], Kuai Yu[3,#], Yuhui Gao[1], Mengdan Chen[1], Dong Duan[1,4], Yunyi Li[2], Xiaoxian Cui[2], Jiabin Mou[2], Yuying Yang[2], Xun Wang[5], Min Chen[2,*], Yaming Jiu[1,*], Jincun Zhao[3,*], Guangxun Meng[1,4,*]

[1]The Center for Microbes, Development and Health, Key Laboratory of Immune Response and Immunotherapy, Shanghai Institute of Immunity and Infection, Chinese Academy of Sciences, University of Chinese Academy of Sciences, Shanghai, 200031, China.

[2]Shanghai Municipal Center for Disease Control and Prevention, Shanghai, 200336, China.

[3]The First Affiliated Hospital of Guangzhou Medical University, State Key Laboratory of Respiratory Disease, National Clinical Research Center for Respiratory Disease, Guangzhou Institute of Respiratory Health, Guangzhou, 510182, China.

[4]Pasteurien College, Soochow University, Suzhou, Jiangsu, 215006, China.

[5]Shanghai Blood Center, Shanghai, 200051, China.

*Corresponding author. Email: Guangxun Meng, gxmeng@ips.ac.cn; Jincun Zhao, zhaojincun@gird.cn; Yaming Jiu, ymjiu@ips.ac.cn; Min Chen, chenmin@scdc.sh.cn

#Authors contributed equally

$Guangzhou National Laboratory, Guangzhou International Bio Island, Guangzhou, Guangdong, 510005, China (Current Address).

Author Contributions: Conceptualization, X.Z., S.Y. and G.M.; Methodology, X.Z., S.Y., Y.J. and G.M.; Investigation, X.Z., S.Y., Y.Z., K.Y., Y.G., Me.C., D.D., Y.L., J.M., X.C., Y.Y., X.W., Y.J. and J.Z.; Writing – Original Draft, X.Z., S.Y.; Writing – Review & Editing, X.Z., S.Y., Y.J. and G.M.; Funding Acquisition, Y.Z., Y.J., M.C. J.Z and G.M.; Resources, Y.J., M.C. J.Z and G.M.; Supervision, G.M.

Competing Interest Statement: Authors declare that they have no competing interests.

Keywords: SARS-CoV-2, innate immune cells, Interlukin-1, cell-cell fusion, actin bundles.

Abstract

Innate immune responses triggered by severe acute respiratory syndrome coronavirus 2 (SARS-CoV-2) infection play pivotal roles in the pathogenesis of COVID-19, while host factors including pro-inflammatory cytokines are critical for viral containment. By utilizing quantitative and qualitative models, we discovered that soluble factors secreted by human monocytes potently inhibit SARS-CoV-2-induced cell-cell fusion in viral-infected cells. Through cytokine screening, we identified that interleukin-1β (IL-1β), a key mediator of inflammation, inhibits syncytia formation mediated by various SARS-CoV-2 strains. Mechanistically, IL-1β activates RhoA/ROCK signaling through a non-canonical IL-1 receptor-dependent pathway, which drives the enrichment of actin bundles at the cell-cell junctions that prevents syncytia formation. Notably, *in vivo* infection experiment in mice confirms that IL-1β significantly restricted SARS-CoV-2 spreading in the lung epithelia. Together, by revealing the function and underlying mechanism of IL-1β on SARS-CoV-2-induced cell-cell fusion, our study highlights an unprecedented antiviral function for cytokines during viral infection.

Main Text

Introduction

The COVID-19 pandemic caused by severe acute respiratory syndrome coronavirus 2 (SARS-CoV-2) infection has spread globally, with at least 755 million people diagnosed and the death toll is over 6.8 million. SARS-CoV-2 variants of concern, including Alpha, Beta, Delta, and Omicron, continue to evolve and increase transmissibility and the ability to escape host immune responses. These variants have brought huge challenges to the design and development of vaccines and therapeutic reagents (Zhou et al., 2020). In order to discover novel strategies to control the virus, it is important to understand host responses to SARS-CoV-2 infection.

SARS-CoV-2 infection induces cell-cell fusion (also known as syncytia formation) in multiple cell types including lung epithelial cells, neurons and glia (Martínez-Mármol et al., 2023). Syncytia of SARS-CoV-2 infected cells with neighboring cells could potentially contribute to increased viral transmission and pathogenicity in the infected host (Rajah, Bernier, Buchrieser, & Schwartz, 2022), which also makes the virus insensitive to extracellular neutralizing antibodies (Li et al., 2022; Yu et al., 2023). Moreover, syncytia formation among pneumocytes with long-term persistence of viral RNA has been observed in the lung autopsy of deceased COVID-19 donors, which may contribute to prolonged clearance of the virus and long COVID symptoms (Bussani et al., 2020). Therefore, inhibiting syncytia formation is critical to ensure viral clearance and to control viral transmission.

It has been reported that SARS-CoV-2 mediated syncytia formation is effectively inhibited by multiple interferon (IFN)-stimulating genes (ISGs) (Pfaender et al., 2020; Wang et al., 2020). However, low IFN levels with impaired ISG responses were observed during early SARS-CoV-2 infection, which may have compromised the antiviral responses of IFN in severe COVID-19 patients (Blanco-Melo et al., 2020; Hadjadj et al., 2020). Thus, identifying endogenous host factors that regulate syncytia formation is of great significance for harnessing the transmission of SARS-CoV-2.

Of note, a variety of cells are involved in the host responses to SARS-CoV-2 infection (Ren et al., 2021), lung epithelial cells are the primary target of SARS-CoV-2 infection and transmission, which subsequently recruit and activate innate immune cells (Barnett et al., 2023). Tissue-resident macrophages and circulating monocytes contribute to local and systemic inflammation largely through releasing inflammatory cytokines (Sefik et al., 2022). Among these cytokines induced by SARS-CoV-2 infection, the combination of TNF-α and IFN-γ induces inflammatory cell death, resulting in clear tissue damage, while other cytokines' function remains obscure (Karki et al., 2021). In addition, when corticosteroids were used to suppress the inflammatory response in patients infected by SARS-CoV (N. Lee et al., 2004) or MERS-CoV (Arabi et al., 2018), the clearance of viral RNA was obviously delayed, suggesting the importance of innate immune factors including cytokines in viral clearance.

Innate immune cells express toll-like receptors (TLRs), and TLR-mediated signaling induces robust production of inflammatory cytokines (Medzhitov, 2001). In the current work, we screened the role of soluble pro-inflammatory cytokines on the SARS-CoV-2 spike-induced cell-cell fusion. Notably, we identified that IL-1β, which is the key factor of inflammatory response, inhibited SARS-CoV-2 spike-induced syncytia formation in various cells by activating RhoA/ROCK pathway to initiate actin bundle formation at cell-cell interface between SARS-CoV-2 infected cells and neighboring cells. Importantly, IL-1β significantly reduced SARS-CoV-2 transmission among lung epithelia in experimental mice *in vivo*. Therefore, our data highlight an important role for pro-inflammatory cytokines against viral infection.

Results

Host factors secreted by activated innate immune cells inhibit SARS-CoV-2 induced cell-cell fusion

We have previously established quantitative and qualitative models for SARS-CoV-2 spike-induced cell-cell fusion by bioluminescence assay, immunoblotting and fluorescence imaging (Yu et al., 2022). In order to explore the potential effect of cytokines on SARS-CoV-2-induced cell-cell fusion, human monocyte cell line THP-1 and human peripheral blood mononuclear cells (PBMCs) were used in this study. We applied several TLR ligands to stimulate such innate immune cells and collected the cell culture supernatants for subsequent experiments **(Fig. 1A)**. Of note, cell culture supernatants of THP-1 cells stimulated by TLR ligands significantly reduced the bioluminescence signal, while neither untreated THP-1 cell culture supernatant nor the medium control had any effect on the bioluminescence signal reflecting cell-cell fusion **(Fig. 1B)**. SARS-CoV-2 spike engagement of ACE2 primed the cleavage of S2' fragment in target cells, a key proteolytic event coupled with spike-mediated membrane fusion (Yu et al., 2022). In parallel with bioluminescence assay, a large amount of enriched S2' cleavage was detected in HEK293T-Spike and HEK293T-ACE2 co-cultured group and co-culture incubated with untreated THP-1 cell culture supernatant, while S2' cleavage was significantly reduced upon treatment with TLR ligands-stimulated THP-1 cell culture supernatants **(Fig. 1C)**. Syncytia formation was also visualized using cells co-expressing spike and a ZsGreen fluorescent reporter. The number and area of syncytium were significantly reduced by the treatment with TLR ligands-stimulated THP-1 cell culture supernatants **(Fig. 1D)**. Considering the presence of TLR ligands in cell culture supernatant, we tested their potential direct effects. As expected, TLR ligands alone did not reduce the bioluminescence signal and S2' cleavage compared to the control groups **(Fig. S1 A and B)**, as well as no effect on syncytia formation **(Fig. S1C)**.

Concurrently, we also tested the effect of PBMCs culture supernatants on SARS-CoV-2 spike-induced cell-cell fusion. Consistent with the results from THP-1 cells, TLR ligands stimulated PBMCs culture supernatants treatment also significantly reduced the bioluminescence signal, S2' cleavage, and the number and area of syncytium compared with the medium group **(Fig. S1 D-F)**. These results suggested that activated innate immune cells released host factors to inhibit SARS-CoV-2 spike-induced cell-cell fusion.

To validate the effect of innate immune cell culture supernatants on cell-cell fusion in authentic SARS-CoV-2 infection, we pre-treated ACE2-expressing cells with THP-1 cell culture supernatants before inoculation with SARS-CoV-2 B.1.617.2 (Delta) or Wuhan-Hu-1 (wild type, WT) strains. Cell lysates were used for the detection of SARS-CoV-2 spike and N protein 24 hours post infection (hpi) **(Fig. 1E)**. This experiment revealed that TLR ligands stimulated THP-1 cell culture supernatants reduced S2' cleavage and N protein during Delta or WT SARS-CoV-2 infection in HEK293T-ACE2 cells, while untreated THP-1 cell culture supernatant had no effect **(Fig. 1F and Fig. S2A)**. In addition, TLR ligands stimulated THP-1 cell culture supernatants significantly reduced the number and area of syncytium induced by Delta or WT SARS-CoV-2 infection **(Fig. S2 B and C)**. Furthermore, we infected the human colon epithelial carcinoma cell line Caco-2 with WT SARS-CoV-2, and found that S2' cleavage and N protein were reduced after TLR ligands stimulated THP-1 cell culture supernatants pre-treatment **(Fig. 1G)**. Accordingly, immunofluorescent staining also showed that TLR ligands stimulated THP-1 cell culture supernatants significantly reduced the number and area of syncytium during SARS-CoV-2 infection in Caco-2 cells **(Fig. 1H)**. These data suggested that host factors secreted by activated innate immune cells inhibit authentic SARS-CoV-2 induced cell-cell fusion.

IL-1β inhibits SARS-CoV-2 induced cell-cell fusion

To explore which host factors inhibited SARS-CoV-2 induced cell-cell fusion, we first detected mRNA levels of different cytokines in THP-1 cells stimulated by TLR ligands. It was found that the

137 expression levels of *IL1A*, *IL1B*, *IL6* and *IL8* were significantly increased upon TLR ligands
138 stimulation, while *IL4*, *IL12A*, *IFNA1*, *IFNB1* and *IFNG* mRNA levels were relatively unchanged or
139 undetected **(Fig. S3A)**. In addition, we also detected the mRNA levels of cytokine receptors in
140 HEK293T modelling cells, confirming that *IL1R1*, *IL4R*, *IL6ST*, *IL8RA*, *IFNAR1*, *IFNGR1* were
141 expressed in such cells, while *IL2RA* and *IL12RB1* were undetectable **(Fig. S3B)**.

142 We next selected recombinant IL-1α, IL-1β, IL-6, and IL-8 to test whether individual cytokine may
143 play a role in affecting SARS-CoV-2 spike induced cell-cell fusion **(Fig. 2A)**. Interestingly, IL-1α
144 and IL-1β significantly reduced the bioluminescence signal compared to the control group, while
145 IL-6 and IL-8 had little or no effect **(Fig. 2B)**. In addition, fluorescence images of cells expressing
146 Zsgreen reporter also confirmed that IL-1α and IL-1β significantly inhibited SARS-CoV-2 spike
147 induced syncytia formation **(Fig. S3C)**. Furthermore, IL-1β and IL-1α both reduced the
148 bioluminescence signal and S2' cleavage **(Fig. 2 C and D, and Fig. S4A)** in cell lysates in a
149 dose-dependent manner. Moreover, the syncytia formation was inhibited with increasing
150 concentrations of IL-1β or IL-1α **(Fig. S4 B and C)**. Intriguingly, when we added both IL-1α and
151 IL-1β, there was no synergistic inhibition on cell-cell fusion compared to either cytokine alone
152 **(Fig. S4 D and E)**, suggesting a potential saturation of IL-1 receptor binding to these
153 homologues. Since both IL-1α and IL-1β activate the downstream pathway through the same
154 receptor IL-1R1, it is suggested that IL-1α or IL-1β may inhibit cell-cell fusion through the same
155 pathway. Considering the higher mRNA level of *IL1B* than *IL1A,* as well as the classical release
156 pathway of IL-1β from innate immune cells (Weber, Wasiliew, & Kracht, 2010), we mainly used
157 IL-1β for further experiments.

158 In order to validate the effect of IL-1β on cell-cell fusion during authentic SARS-CoV-2 infection,
159 we pre-treated ACE2-expressing cells with IL-1β before inoculating with Delta or WT authentic
160 SARS-CoV-2. Cell lysates were used for the detection of SARS-CoV-2 spike and N protein 24 hpi
161 **(Fig. 2E)**. To this end, it was found that IL-1β reduced S2' cleavage and N protein compared to
162 the control group during such infection both in HEK293T-ACE2 **(Fig. 2F and Fig. S5A)** and Caco-
163 2 cells **(Fig. 2G)**. Meanwhile, IL-1β inhibited authentic SARS-CoV-2 induced syncytia formation
164 **(Fig. 2H and Fig. S5 B and C)**. These results verified that IL-1β inhibits authentic SARS-CoV-2
165 induced cell-cell fusion in various target cells.

166 As expected, innate immune cells activated by TLR ligands secreted IL-1β into the cell culture
167 supernatants **(Fig. S6, A and B),** and TLR2 was essential for THP-1 cells to release IL-1β in
168 response to TLR2 ligands **(Fig. S6C)**. More importantly, the cell culture supernatants of TLR2-
169 knockout THP-1 cells stimulated by TLR2 Ligands had no effect on the bioluminescence signal,
170 while the cell culture supernatants from WT THP-1 cells stimulated by the same TLR2 Ligands
171 significantly reduced the bioluminescence signal **(Fig. S6D)**. In addition, pre-treatment with TAK1
172 inhibitor (5Z-7) or IKKβ inhibitor (TPCA1) in WT THP-1 cells prevented IL-1β secretion after PGN
173 stimulation **(Fig. S6E)**, as well as eliminated the inhibitory effect of PGN-stimulated WT THP-1
174 cell culture supernatant on SARS-CoV-2 spike-induced cell-cell fusion **(Fig. S6F)**. In parallel, pre-
175 treatment with these inhibitors in PBMCs showed the same results **(Fig. S6 G and H)**. These
176 data suggested that TLR-knockout or inhibitors targeting the respective TLR signaling prevented
177 innate immune cells from releasing IL-1β into supernatants, which led to failed inhibition of SARS-
178 CoV-2 spike induced cell-cell fusion. These findings thus further verify that IL-1β is an important
179 host factor inhibiting SARS-CoV-2 induced cell-cell fusion.

180 To investigate the effector function of IL-1 on cells expressing SARS-CoV-2 spike (donor cells)
181 and neighboring cells expressing ACE2 (acceptor cells), we pre-treated HEK293T-S or
182 HEK293T-ACE2 cells or both with IL-1β, then co-cultured after washing with PBS. Cells were
183 then analyzed by the quantitative and qualitative models **(Fig. S7A)**. Notably, pre-treatment of
184 either HEK293T-S or HEK293T-ACE2 cells with IL-1β alone reduced bioluminescence signal and
185 S2' cleavage; when IL-1β pre-treatment on both HEK293T-S and HEK293T-ACE2 cells was
186 applied, bioluminescence signal and S2' cleavage were further reduced **(Fig. S7B)**. Furthermore,
187 we used Vero E6-overexpressing ACE2 cell line (Vero E6-ACE2) and human Calu-3 cells as

188 acceptor cells. In this case, pre-treatment of either HEK293T-S or Vero E6-ACE2 cells with IL-1β
189 alone reduced part of S2' cleavage, while IL-1β pre-treatment of both HEK293T-S and Vero E6-
190 ACE2 cells led to further reduction of S2' cleavage **(Fig. S7C)**. And the same results were
191 observed in the case of Calu-3 as acceptor cells **(Fig. S7D)**. Accordingly, fluorescence imaging
192 showed that IL-1β significantly reduced the number and area of syncytia **(Fig. S8A)**. Notably, IL-
193 1β reduced the bioluminescence signal and S2' cleavage in different SARS-CoV-2 variants **(Fig.**
194 **S8 B-D)**. These results suggest that IL-1β acts on both donor and acceptor cells to inhibit SARS-
195 CoV-2 spike induced cell-cell fusion in various cell lines.

196 SARS-CoV (Belouzard, Chu, & Whittaker, 2009) and MERS-CoV (Straus et al., 2020) spike
197 protein also induce cell-cell fusion in target cells. Therefore, we further explored whether IL-1β
198 could also inhibit SARS-CoV and MERS-CoV spike-induced cell-cell fusion in ACE2- or Dipeptidyl
199 peptidase-4 (DPP4)-expressing cells by bioluminescence assay, immunoblotting and a modified
200 *stop-mCherry* fluorescent model, wherein mCherry reporter is only expressed when Cre excises
201 the Stop cassette inside the fused syncytia **(Fig. S9A)**. Similar to SARS-CoV-2 spike-induced
202 cell-cell fusion, IL-1β also reduced bioluminescence signal **(Fig. S9 B and C)**, S2' cleavage **(Fig.**
203 **S9 D and E)** and the number and area of syncytium **(Fig. S9F)**. These data suggested that IL-1β
204 possesses a broad spectrum to inhibit cell-cell fusion induced by different coronaviruses.

205 **IL-1β inhibits SARS-CoV-2 induced cell-cell fusion through IL-1R1/MyD88/IRAK/TRAF6**
206 **pathway**

207 To investigate the mechanism of IL-1β inhibition on SARS-CoV-2 induced cell-cell fusion, we
208 performed gene knockout using CRISPR-Cas9 technology, in conjunction with inhibitors targeting
209 the IL-1 receptor pathway **(Fig. 3A)**. In the presence of IL-1 receptor antagonist (IL-1RA), IL-1β
210 was unable to reduce bioluminescence signal and S2' cleavage **(Fig. 3B)**. MyD88 is the
211 downstream adaptor of IL-1R1. We then generated MyD88 knockout HEK293T cell line, wherein
212 IL-1β was unable to reduce bioluminescence signal **(Fig. 3C)** and S2' cleavage **(Fig. S10A)**. In
213 addition, we found that IL-1β was unable to reduce bioluminescence signal and S2' cleavage in
214 the presence of IRAK1/4 inhibitor **(Fig. 3D)**. Furthermore, IL-1β was also unable to reduce
215 bioluminescence signal **(Fig. 3E)** and S2' cleavage **(Fig. S10B)** in TRAF6 knockout HEK293T cell
216 line. These results suggested that IL-1β inhibits SARS-CoV-2 spike induced cell-cell fusion
217 through IL-1R1-MyD88-IRAK-TRAF6 pathway.

218 Intriguingly, when we tested TAK1, a downstream molecule of TRAF6 for the potential
219 involvement in the signaling, it was found that IL-1β still reduced bioluminescence signal and S2'
220 cleavage in TAK1 knockout (sgMAP3K7) HEK293T cell line **(Fig. S11A)**. Moreover, we found that
221 in the presence of TPCA1, an IKKβ inhibitor, IL-1β still inhibited bioluminescence signal and S2'
222 cleavage as well **(Fig. S11B)**. Although IL-1β upregulates the mRNA transcription levels of NF-κB
223 pathway-related genes, such as *RELB*, *NFKBIA*, and *NFKB1* **(Fig. S11C)**, IL-1β still reduced the
224 bioluminescence signal after these NF-κB pathway-related genes knockout **(Fig. S11D)**. Taken
225 together, these results demonstrated that IL-1β inhibits SARS-CoV-2 spike induced cell-cell
226 fusion independent from the TAK1-IKKβ-NF-κB signaling cascade.

227 Furthermore, we validated these findings in authentic SARS-CoV-2 infected Caco-2 and Calu-3
228 cells. Consist with the results from HEK293T cells, IL-1β failed to reduce S2' cleavage and N
229 protein in the presence of IRAK1/4 inhibitor, whereas it still reduced S2' cleavage and N protein in
230 the presence of the IKKβ inhibitor TPCA1 in Caco-2 **(Fig. 3F)** and Calu-3 cells **(Fig. 3G)**.

231 **IL-1β inhibits SARS-CoV-2 induced cell-cell fusion through RhoA/ROCK mediated actin**
232 **bundle formation at the cell-cell junction**

233 It has been reported that IL-1β activates RhoA signaling via MyD88 and IRAK, which is a
234 pathway independent from IKKβ (Chen, Zuraw, Liu, Huang, & Pan, 2002). As a major
235 downstream effector of RhoA, ROCK phosphorylates substrates that are involved in the

236 regulation of the actin cytoskeleton, cell attachment, and cell motility (Riento & Ridley, 2003).
237 Therefore, we set out to detect the active level of RhoA through pull-down assay. To this end, we
238 verified that IL-1β activated RhoA signaling in sgControl HEK293T cells but not in sgMyD88- or
239 sgTRAF6-HEK293T cells **(Fig. 4A)**. To directly visualize the distribution of endogenous GTP-
240 RhoA (active RhoA), we used a location biosensor derived from the carboxy terminus of anillin
241 (GFP-AHPH) (Priya et al., 2015; Sun et al., 2015). Interestingly, IL-1β significantly increased the
242 fluorescence intensity of GFP-AHPH in sgControl HEK293T cells, but had no effect in sgMyD88-
243 and sgTRAF6-HEK293T cells **(Fig. 4 B and C)**.

244 To investigate whether IL-1β inhibits SARS-CoV-2 spike-induced cell-cell fusion through
245 RhoA/ROCK pathway, we co-transfected GFP-AHPH in ACE2-expressing cells, then co-cultured
246 with S-expressing cells at different time points. In the process of syncytia formation, cell-cell
247 contact established between S-expressing cells and ACE2-expressing cells, and GFP-AHPH
248 localized distally from cell-cell junction in the early stage of syncytia formation. With the
249 enlargement of syncytium, GFP-AHPH is visualized at the periphery of syncytium **(Fig. 4D, top**
250 **panel)**. However, in IL-1β treated group, GFP-AHPH foci is enriched to the cell-cell junction in the
251 early stage. Over time, GFP-AHPH was recruited more to the cell-cell junction between S-
252 expressing cells and ACE2-expressing cells, preventing further cell-cell fusion **(Fig. 4D, bottom**
253 **panel)**. Cartoon schematics inserted in the imaging data illustrate such findings in a modeled
254 manner.

255 ROCK-mediated actin rearrangement is through the downstream substrates, which induces
256 cross-linking of actin bundles with myosin and generate contractile forces along these bundles
257 (Watanabe, Kato, Fujita, Ishizaki, & Narumiya, 1999). It has been reported that RhoA initiates
258 actin arc formation (Dupraz et al., 2019; Stern et al., 2021), so we further explored the changes of
259 actin cytoskeleton during SARS-CoV-2 spike-induced cell-cell fusion. Phalloidin staining showed
260 that actin filaments (F-actin) at cell-cell junction between S-expressing cells and ACE2-
261 expressing cells was gradually disappeared along with cell-cell fusion in the early stages of
262 syncytia formation. With the formation and enlargement of syncytium, F-actin of syncytium is
263 preferably distributed peripherally **(Fig. 4E, top panel)**. However, IL-1β activated RhoA to initiate
264 actin bundles formation at cell-cell junction, the formation of these actin bundles potentially
265 generates barriers and prevents membrane fusion between S-expressing cells and ACE2-
266 expressing cells. Even with the prolonged co-culture time, IL-1β-induced actin bundles formed at
267 cell junctions consistently inhibited further syncytia formation **(Fig. 4E, bottom panel)**.

268 Consistent with our previous results, immunofluorescence staining showed GFP-AHPH moving to
269 the opposite of cell-cell junction and locating peripherally with syncytia formation **(Fig. 4F, top**
270 **panel)**, while upon IL-1β treatment, GFP-AHPH located at the cell-cell junction of authentic
271 SARS-CoV-2 infected cells and neighboring cells **(Fig. 4F, bottom panel)**. In parallel, staining
272 results showed that F-actin at the cell-cell junction were disassembled during authentic SARS-
273 CoV-2 infection; with the formation of syncytium, F-actin of syncytium was mainly distributed
274 peripherally **(Fig. 4G, top panel)**. However, actin bundles formed at cell-cell junction induced by
275 IL-1β inhibited membrane fusion and further syncytia formation **(Fig. 4G, bottom panel)**.
276 Furthermore, we also observed the same results in authentic SARS-CoV-2 infected Caco-2 cells.
277 F-actin of syncytium in control group was also distributed peripherally, the formation of syncytium
278 promoted the transmission of SARS-CoV-2, as N protein was widely distributed in the cytoplasm
279 of the syncytium **(Fig. 4H, top panel)**. While in IL-1β treated group, actin bundles formed at cell-
280 cell junction between SARS-CoV-2 infected cells and neighboring cells prevented syncytia
281 formation and further viral transmission **(Fig. 4H, bottom panel)**. Together, these data revealed
282 that IL-1β induced the formation of actin bundles at the cell-cell junction of SARS-CoV-2 infected
283 cells and neighboring cells through RhoA/ROCK pathway, which inhibited SARS-CoV-2 induced
284 cell-cell fusion.

285 To further investigate the role of RhoA/ROCK pathway in inhibiting SARS-CoV-2 induced cell-cell
286 fusion, we co-transfected constitutively activated RhoA L63 (Nobes & Hall, 1999) (RhoA-CA)

287 plasmid with spike or ACE2 in HEK293T cells, and found that RhoA-CA significantly reduced the
288 bioluminescence signal and S2' cleavage in a dose-dependent manner **(Fig. 5A)**. HEK293T-
289 ACE2 **(Fig. S12A)**, Caco-2 **(Fig. 5B)** and Calu-3 cells **(Fig. 5C)** expressing RhoA-CA also
290 significantly reduced S2' cleavage and N protein compared to the control group during authentic
291 SARS-CoV-2 infection. Meanwhile, we observed that constitutive activation of RhoA enriches
292 actin bundles at cell-cell junction, thus preventing SARS-CoV-2 induced cell-cell fusion in
293 HEK293T-ACE2 **(Fig. S12B)**, Caco-2 **(Fig. 5D)** and Calu-3 cells **(Fig. 5E)**.

294 ROCK inhibitor Y-27632 treatment prevents the formation of actin bundles (van der Heijden et al.,
295 2008), so we hypothesized that Y-27632 could affect the inhibitory effect of IL-1β on SARS-CoV-
296 2 spike-induced cell-cell fusion. Indeed, Y-27632 treatment increased bioluminescence signal and
297 S2' cleavage in a dose-dependent manner, promoting syncytia formation. When treated with
298 lower concentrations of Y-27632, IL-1β can eliminate Y-27632-enhanced cell-cell fusion.
299 However, IL-1β was unable to inhibit cell-cell fusion in the presence of higher concentrations of Y-
300 27632 **(Fig. S12C)**. Immunofluorescence results showed that although IL-1β induced actin
301 bundles inhibited cell-cell fusion **(Fig. S12D, top panel)**, higher concentrations of ROCK inhibitor
302 Y-27632 treatment prevented the formation of IL-1β-induced actin bundles at cell-cell junctions,
303 promoting membrane fusion and cytoplasmic exchange between S-expressing cells and ACE2-
304 expressing cells, which restored syncytia formation **(Fig. S12D, bottom panel)**. Furthermore, we
305 verified that IL-1β was unable to reduce S2' cleavage and N protein in the presence of Y-27632 in
306 authentic SARS-CoV-2 infected Caco-2 **(Fig. 5F)**, Calu-3 cells **(Fig. 5G)** and human lung cells
307 **(Fig. 5H)**. Immunofluorescence results also confirmed that the elimination of IL-1β induced actin
308 bundles by Y-27632 in Caco-2 **(Fig. 5I)** and Calu-3 cells **(Fig. 5J)**. These results indicated that
309 preventing the formation of RhoA/ROCK mediated actin bundles at cell-cell junction promotes
310 SARS-CoV-2 induced cell-cell fusion.

311 **IL-1β restricts SARS-CoV-2 transmission via induction of actin bundles *in vivo***

312 To demonstrate the role of IL-1β in controlling SARS-CoV-2 transmission *in vivo*, BALB/c mice
313 were infected with authentic SARS-CoV-2 B.1.351 after IL-1β or IL-1RA+IL-1β pre-treatment **(Fig.**
314 **S13A)**. Interestingly, the results of this experiment showed that in mice with IL-1β treatment, the
315 body weight loss was less than in the control group, while IL-1β was unable to improve body
316 weight in the presence of IL-1RA **(Fig. S13B)**. According to hematoxylin and eosin (H&E)
317 staining, tissue histopathology analysis demonstrated that the mice with IL-1β treatment carry
318 less pulmonary injury compared to the control and IL-1RA+IL-1β group **(Fig. 6 A and B)**. In
319 addition, the expression level of SARS-CoV-2 N gene in the lung from IL-1β treated mice was
320 significantly lower than in the control and IL-1RA+IL-1β treated mice **(Fig. 6C)**. In addition,
321 immunohistochemistry staining showed that the infected area in the epithelial linings of lung
322 tissue was significantly reduced by IL-1β treatment compared to the control and IL-1RA+IL-1β
323 groups **(Fig. 6 D and E)**, indicating that IL-1β restricted the transmission of SARS-CoV-2 in the
324 lung. Moreover, fluorescence staining showed that SARS-CoV-2 infected lung epithelial cells
325 fused with neighboring cells, promoting viral transmission in the airway epithelial cells, while IL-1β
326 induced the formation of actin bundles to restrict the syncytia formation and further viral
327 transmission **(Fig. 6F, Fig. S13 C and D)**.

328 To further verify the function and mechanism of IL-1β in controlling SARS-CoV-2 transmission,
329 we treated BALB/c mice with PBS, IL-1β or ROCK inhibitor Y-26732 + IL-1β **(Fig. S14A)**, then
330 isolated the lung tissue cells for authentic SARS-CoV-2 infection. We found that S2' cleavage and
331 N protein were significantly reduced in IL-1β treated mice compared to control mice at day 2,
332 while Y-26732 treatment abolished the inhibitory effect of IL-1β on S2' cleavage and N protein
333 **(Fig. 6G)**. Of note, the lung tissue cells in IL-1β treated mice remained resistant to SARS-CoV-2
334 infection at day 7, while the protective effect of IL-1β was abolished by Y-26732 treatment **(Fig.**
335 **S14B)**.

336 In addition, we found that IL-1β treated mice have no significant changes in body weight, liver and
337 spleen weight compared to control mice **(Fig. S15 A-D)**, indicating that this dose of IL-1β did not
338 cause toxicity. Of note, we isolated the tissue cells and then infected with authentic SARS-CoV-2,
339 the results showed that S2' cleavage and N protein were significantly reduced in IL-1β treated
340 mice compared to control mice both in isolated lung and intestine tissue cells **(Fig.S15 E and F)**,
341 suggesting that IL-1β may have protective effects on various tissue cells during SARS-CoV-2
342 infection. Taken together, IL-1β prevents the transmission of SARS-CoV-2 *in vivo* by inducing the
343 formation of actin bundles.

Discussion

In the present study, we explored the functional roles of innate immune factors against SARS-CoV-2 infection. Notably, IL-1β inhibited various SARS-CoV-2 variants and other beta-coronaviruses spike-induced cell-cell fusion. Mechanistically, IL-1β activates and enriches RhoA to the cell-cell junction between SARS-CoV-2-infected cells and neighboring cells via the IL-1R-mediated signal to initiate actin bundle formation, preventing cell-cell fusion and viral spreading (**Fig. S16**). These findings revealed a critical antiviral function for pro-inflammatory cytokines to control viral infection.

Elevated IL-1β levels in severe COVID-19 patients is central to innate immune response as it induces the expression of other pro-inflammatory cytokines (Tahtinen et al., 2022). In addition, IL-1α is also secreted during SARS-CoV-2 infection (Xiao et al., 2021). Of note, several therapeutic strategies have employed the inhibition of IL-1 signal in an attempt to treat SARS-CoV-2 infection (Huet et al., 2020; Ucciferri et al., 2020). Intriguingly, although anakinra, a recombinant human IL-1 receptor antagonist, improved clinical outcomes and reduced mortality in severe COVID-19 patients (Cavalli et al., 2020), it did not reduce mortality in mild-to-moderate COVID-19 patients, and even increased the probability of serious adverse events (Tharaux et al., 2021). With another note, IL-1 blockade significantly decreased the neutralizing activity of serous anti-SARS-CoV-2 antibodies in severe COVID-19 patients (Della-Torre et al., 2021). According to our finding that both IL-1β and IL-1α are able to inhibit SARS-CoV-2-induced cell-cell fusion, inhibition of IL-1 signaling may have abolished the antiviral function of IL-1, thus failing to restrict virus-induced syncytia formation and transmission.

Notably, IL-1β plays a key role in triggering vaccine-induced innate immunity, suggesting that innate immune responses play important roles in the antiviral defense by enhancing the protective efficacy of vaccines (Eisenbarth, Colegio, O'Connor, Sutterwala, & Flavell, 2008; Tahtinen et al., 2022). In addition, vaccination with Bacillus Calmette-Guérin (BCG) has been reported to confer nonspecific protection against heterologous pathogens, including protection against SARS-CoV-2 infection in human and mice (Hilligan et al., 2022; A. Lee et al., 2023; Rivas et al., 2021). In addition, Lipid nanoparticle (LNP) in mRNA vaccine (Han et al., 2023) and penton base in adenovirus vaccine (Di Paolo et al., 2009) can both activate innate immune cells to amplify the protective effect of vaccines, which may also be attributed to IL-1β-mediated inhibition of SARS-CoV-2-induced cell-cell fusion on top of adaptive immune responses induced by the vaccines.

With another note, patients with inherited MyD88 or IRAK4 deficiency have been reported to be selectively vulnerable to COVID-19 pneumonia. It was found that these patients' susceptibility to SARS-CoV-2 can be attributed to impaired type I IFN production, which do not sense the virus correctly in the absence of MyD88 or IRAK4 (García-García et al., 2023). In our study, MyD88 or IRAK4 deficiency abolished the inhibitory effect of IL-1β on SARS-CoV-2 induced cell-cell fusion, suggesting that these innate immune molecules are critical to contain SARS-CoV-2 infection, and this may be another mechanism accounting for the disease of those patients. Moreover, MyD88 signaling was essential for BCG induced innate and type 1 helper T cell (TH1 cell) responses, and protection against SARS-CoV-2, which is consistent with our fundings.

Of note, cell-cell fusion is not limited to the process of viral infection, both normal and cancerous cells can utilize this physiological process in tissue regeneration or tumor evolution (Delespaul et al., 2020; Powell et al., 2011). For example, myoblast fusion is the key process of skeletal muscle terminal differentiation, inactivation of RhoA/ROCK signaling is crucial for myoblast fusion (Nishiyama, Kii, & Kudo, 2004). Our current work revealed that inhibition of RhoA/ROCK signaling promoted virus-induced cell-cell fusion, possibly due to the virus hijacking of such biological process. In turn, activated RhoA/ROCK signaling inhibits virus-induced cell-cell fusion, so it can be targeted for future therapeutic development to control viral transmission. Cell-cell fusion is mediated by actin cytoskeletal rearrangements, the dissolution of F-actin focus is essential for

395 cell-cell fusion; in contrast, syncytia formation cannot proceed if disassembly of actin filaments or
396 bundles is prevented (Doherty et al., 2011; Rodríguez-Pérez et al., 2021). We uncovered that
397 preventing actin bundles dissolution inhibited virus-induced cell-cell fusion, and IL-1β induced
398 RhoA/ROCK signal promotes actin bundle formation at cell-cell junctions. As RhoA is ubiquitously
399 expressed by all cell types, it is currently unclear whether IL-1-mediated RhoA activation is
400 specific towards viral infection-associated cytoskeleton modification, or may regulate other RhoA-
401 related processes, which is a limitation of the current work and remains to be investigated in
402 future.

403 In summary, this study demonstrated the function and mechanism of IL-1β in inhibiting SARS-
404 CoV-2 induced syncytia formation, and highlighted the function of innate immune factors including
405 cytokines against coronaviruses transmission, thus provide potential therapeutic targets for viral
406 control.

Materials and Methods

Reagents and plasmids

The antibodies used for immunoblotting include: rabbit anti-SARS-CoV-2 S2 (Sino Biological, 40590-T62, 1:2000), mouse anti-SARS-CoV-2 N (Sino Biological, 40143-MM05, 1:1000), rabbit anti-ACE2 (Proteintech, 21115-1-AP, 1:2000), rabbit anti-MERS-CoV S2 (Sino Biological, 40070-T62, 1:1000), rabbit anti-MyD88 (Cell Signaling Technology, 4283, 1:1000), rabbit anti-TRAF6 (Abcam, ab33915, 1:5000), rabbit anti-TAK1 (Cell Signaling Technology, 4505, 1:1000), mouse anti-Myc-Tag (Abclonal, AE010,1:2000), HRP-conjugated β-tubulin (Abclonal, AC030, 1:5000), mouse anti-β-actin (Proteintech, 66009-1-Ig, 1:5000), anti-rabbit/anti-mouse (Jackson Immuno Research, 111-035-003, 1:5000). The antibodies and regents used for immunofluorescence include: rabbit anti-SARS-CoV-2 S2 (Sino Biological, 40590-T62, 1:200), mouse anti-SARS-CoV-2 N (Sino Biological, 40143-MM05, 1:200), rabbit anti-ACE2 (Proteintech, 21115-1-AP, 1:200), mouse anti-HA-Tag (Abclonal, AE008, 1:200). Actin-Tracker Green-488 (Beyotime, C2201S,1:100), goat α-mouse IgG-555 (Invitrogen, A-21424, 1: 400) and goat α-rabbit IgG-647 (Invitrogen, A-21236, 1: 400), DAPI (Abcam, ab228549, 1:2000) and antifade mounting medium (vectorlabs, H-1400-10). Purified LTA from S. aureus (Invitrogen, tlrl-pslta), Pam3CSK4 (Invitrogen, tlrl-pms), Peptidoglycan from S. aureus (Sigma-Aldrich, 77140), LPS (Invitrogen, tlrl-eklps), TPCA1 (Selleck, S2824), 5Z-7-Oxozeaenol (Sigma-Aldrich, O9890), IRAK1/4 inhibitor (Selleck, S6598), Y-27632 (Selleck, S6390). Inhibitors were dissolved in dimethyl sulfoxide (DMSO, Sigma-Aldrich, D2650), and DMSO was added as solvent control. Recombinant human IL-1α (200-01A), human IL-1β (200-01B), mouse IL-1β (211-11B), human IL-1RA (200-01RA), human IL-6 (200-06) and human IL-8 (200-08M) were purchased from Peprotech. mouse IL-1RA (769706) was purchased from BioLegend. IL-1β concentrations in supernatants from THP-1 and PBMCs were determined using ELISA kits, according to the manufacturer's instructions (R&D Systems, DY201). RhoA pull-down activation assay Biochem Kit (BK036-S) was purchased from Cytoskeleton, Inc. Collagenase, type I (17100017) was purchased from Gibco and B-ALI Growth Media (00193516) was purchased from Lonza Bioscience.

SARS-CoV-2 spike (Wuhan-Hu-1, GenBank: QHD43419.1) was homo sapiens codon-optimized and generated *de novo* into pVAX1 vector by recursive polymerase chain reaction (PCR). WT, Alpha, Beta and Delta variants containing point and deletion mutations were generated using stepwise mutagenesis using spike construct containing the truncated 19 amino acids at the C-terminal (CTΔ19). The latest human codon optimized Omicron was purchased from Genescripts, and subcloned into the pVAX1 backbone with CTΔ19 for comparison. Human ACE2 assembled in a pcDNA4.0 vector was used for transient expression of ACE2. GFP-AHPH (Addgene plasmid # 71368; http://n2t.net/addgene:71368; RRID: Addgene_71368) and pRK5myc RhoA L63 (Addgene plasmid # 15900; http://n2t.net/addgene:15900; RRID: Addgene_15900) were from Addgene.

Cell culture and stimulation

HEK293T cells were purchased from the National Science & Technology Infrastructure (NSTI) cell bank (www.cellbank.org.cn). Caco-2 cells (catalog no. SCSP-5027) were obtained from Cell Bank/Stem Cell Bank, Chinese Academy of Sciences. Vero E6-ACE2 and Calu-3 cells were gifted from Prof. Dimitri Lavillette (Applied Molecular Virology Laboratory, Discovery Biology Department, Institut Pasteur Korea). HEK293T and Vero E6-ACE2 were cultured in Gibco Dulbecco's Modified Eagle Medium (DMEM) (GE Healthcare) supplemented with 10% fetal bovine serum (FBS) (Sigma) and 1% Penicillin/streptomycin (P/S) (Life Technologies) at 37°C with 5% CO_2 in a humidified incubator. Human colon epithelial carcinoma cell line Caco-2 and human lung cancer cell line Calu-3 cells were cultured in Minimum Essential Medium (MEM) supplemented with 10% FBS, 1% non-essential amino acids and 1% P/S at 37°C with 5% CO_2 in a humidified incubator. Human monocytic cell line THP-1 was cultured in Roswell Park Memorial Institute (RPMI) 1640 supplemented with 10% FBS, 1% P/S and 50 μM 2-ME at 37°C with 5%

457 CO_2 in a humidified incubator. All cells were routinely tested for mycoplasma contamination;
458 passages between 4 th to 25 th were used. Human PBMCs were isolated from the peripheral blood
459 of healthy doners (Shanghai Blood Center). This study was performed in accordance with the
460 International Ethical Guidelines for Biomedical Research Involving Human Subjects and the
461 principles expressed in the Declaration of Helsinki. Briefly, fresh human PBMCs were separated
462 using Ficoll-Paque PLUS reagent (cytiva, 17144003) at 1200 g for 10 min at room temperature
463 with SepMateTM-50 (SepMate, 86450). PBMCs were washed three times with filtered PBS
464 containing 0.5% BSA and 2 mM EDTA. PBMCs was counted and resuspended in RPMI 1640
465 medium supplemented with 1% FBS and 1% P/S.

466 For stimulation, THP-1 cells were seeded at 2×10^6 cells per ml in FBS free RPMI 1640 and
467 PBMCs were seeded at 1×10^7 cells per ml in 1% FBS RPMI 1640, then stimulated with LTA (10
468 μg/ml), Pam3CSK4 (1 μg/ml), PGN (2 μg/ml), LPS (1 μg/ml) for 24 hours, cell culture
469 supernatants were collected after centrifugation at 2000 g for 5 min for subsequent experiments.

470 **Transient transfection and cell-cell fusion assays**

471 For transient transfections, HEK293T cells were seeded in flat bottom 24-well plates at 0.5×10^6
472 cells /mL overnight. 250 ng plasmids encoding SARS-CoV-2 spike mutants or ACE2 variants
473 were packaged in Lipofectamine 2000 (Life technologies) and transfected for 24 hours. For
474 luciferase assays, S-mediated membrane fusion, a *Cre-loxp* Firefly luciferase (*Stop-Luc*) co-
475 expression system was introduced to enable the detection of DNA recombination events during
476 cell-cell-cell fusion. 200 ng Cre plasmids were co-transfected into S-HEK293T cells and 200 ng
477 *Stop-Luc* plasmid were co-transfected into ±ACE2-HEK293T cells, respectively. For visualization
478 of syncytia formation, 100 ng ZsGreen plasmid was co-transfected with spike variants. HEK293T
479 cells in the 24-well plates were then detached using ice-cold calcium-free PBS in the absence of
480 trypsin and centrifuged at 600 g for 4 min.

481 For cell-cell fusion assays, cell pellets were resuspended into complete DMEM and mixed with
482 control HEK293T cells, or HEK293T-ACE2, Vero E6-ACE2 or Calu-3 cells at 1:1 ratio before
483 adhesion to the 48-well or 96-well plates, cell mixes were incubated for 16 hours at 37°C.
484 Quantification of cell-cell-cell fusion was performed by measuring luciferase expression as
485 relative luminescence units (RLU) 1 min by mixing cell lysates with the Steady-Glo luciferase
486 substrate (E2520, Promega) on a Synergy H1 plate reader (Biotek). Fluorescent images showing
487 syncytia formation were captured at endpoint using a 10x objective and 12-bit monochrome
488 CMOS camera installed on the IX73 inverted microscope (Olympus). Attached cells and syncytia
489 were lysed in a NP-40 lysis buffer containing 0.5% (v/v) NP-40, 25 mM Tris pH 7.3, 150 mM
490 NaCl, 5% glycerol and 1x EDTA-free protease inhibitor cocktail (PIC) (Roche).

491 **Immunoblotting**

492 Tissue culture plates containing adherent syncytia and cell mixes were directly lysed on ice in 2x
493 reducing Laemmli loading buffer before boiled at 95°C for 5 min. Protein samples were separated
494 by standard Tris-glycine SDS-PAGE on 7.5% or 9.5% Tris-glycine polyacrylamide gels. Proteins
495 were then transferred onto 0.45 μm PVDF membranes (Millipore) for wet transfer using Towbin
496 transfer buffer. All membranes were blocked in PBS supplemented with 0.1% Tween20 (PBST)
497 and 2.5% bovine serum albumin (BSA) or 5% non-fat dry milk, before overnight incubation in
498 primary antibodies at 4°C. Blots were labelled with HRP-tagged secondary antibodies (Jackson
499 ImmnuoResearch) and visualized with PicoLight substrate enhanced chemiluminescence (ECL)
500 solution (Epizyme Scientific). Immunoblot images were captured digitally using a 5200
501 chemiluminescent imaging system (Tanon) with molecular weight markers indicated.

502 **Real time PCR**

503 HEK293T cells of 0.5 x 10^6 cells /mL were inoculated in 24 wells overnight. After the cells were
504 about 80% covered, the specified stimulant was added, washed with PBS for three times, and 1
505 mL TRIzol Reagent (15596018; Thermo Fisher Scientific) was added for full lysis at room
506 temperature for 5 min, add 250 μL chloroform fully mixed at room temperature for 5 min,
507 centrifuge at 10000 r/min, centrifuge at 4°C for 10 min. Carefully remove the aqueous phase
508 using a pipette. Leave behind some of the aqueous phase (about 1 mm above DNA layer to
509 prevent DNA contamination). Place in another 1.5 mL Eppendorf tube. Add 550 μl isopropanol to
510 the aqueous phase and mix gently. Leave at -20°C for 30 min. 14000 r/min, centrifuge at 4°C for
511 20 min, wash with 75% ethanol twice. Dissolve in 30 μL DEPC water. Then reverse transcribed to
512 cDNA using a GoSript Reverse Transcription kit (Promega). Real-time PCR was performed using
513 SYBR Green Realtime PCR Master Mix (TOYOBO) on ABI QuantStudio 6 flex Real-time PCR
514 System (Thermo Fisher Scientific). The RT-qPCR Primer sequences for targeting respective
515 genes are displayed in Table S1. Target genes Relative quantification were normalized to
516 GAPDH as relative unit (RU) via formula.

517 **CRISPR/Cas9-Mediated Gene Targeting**

518 Gene-deficient THP-1 or HEK293T cells were generated using CRISPR/Cas9-mediated gene
519 targeting technology. Briefly, LentiCRISPR v2 (52961; addgene) containing sgRNA specifically
520 targeting indicated genes were constructed. The sgRNA sequences for targeting respective
521 genes are displayed in Table S2. The Lentiviral particles were produced in HEK293T cells by
522 transfection with LentiCRISPR v2-sg gene, psPAX2, VSV-G at 2:1.5:1 ratio using Lipofectamine
523 2000. The lentiviral particles were then used to infect THP-1 or HEK293T cells. One day post
524 infection, the cells were subjected to puromycin selection at a concentration of 2 μg/ml for 72
525 hours. Surviving cells were subjected to limiting dilution and seed in 96-well plates to obtain
526 single clones stably knocking out respective genes.

527 **RhoA pull-down assay**

528 After 1 ng/mL IL-1β treatment for 30 min, place culture vessel on ice, aspirate media, wash with
529 ice cold PBS. Aspirate off PBS. Tilt plates on ice for an additional 1 min to remove all remnants of
530 PBS. Residual PBS will adversely affect the assay. Lysis cells in an ice-cold cell lysis buffer with
531 protease inhibitor cocktail. Harvest cell lysates with a cell scraper. Transfer lysates into the pre-
532 labeled sample tubes on ice. Immediately clarify by centrifugation at 10000 g, 4°C for 1 min. Save
533 20 μL of lysate for total RhoA. For pulldown assay, add 600 μg total cell protein to 10 μL rhotekin-
534 RBD beads, then incubate at 4°C on a rotator for 1 hour. Pellet the rhotekin-RBD beads by
535 centrifugation at 5000 g at 4°C for 1 min. Very carefully remove 90% of the supernatant, then
536 wash the beads once with 500 μL each of Wash Buffer. Pellet the rhotekin-RBD beads by
537 centrifugation at 5000 g at 4°C for 3 min. Very carefully remove the supernatant. Add 20 μL of 2x
538 Laemmli sample buffer to each tube and thoroughly resuspend the beads. Boil the bead samples
539 for 2 min. The samples were analyzed by Immunoblots.

540 **Immunostaining and confocal microscopy**

541 HEK293T cells were seeded overnight onto sterilized poly-D-lysine (100 ug/mL) (Beyotime,
542 ST508) treated 12 mm coverslips (fisher scientific, 1254580) in 24-well plates. After transfection
543 with spike mutants, cells were washed with PBS once before fixed with 4% (w/v)
544 paraformaldehyde (PFA) for 20 min. Then, cells were washed twice with PBS and permeabilized
545 by 0.1% Triton at room temperature for 10 min. Next, cells were washed twice with PBS and
546 blocked with Immunol Staining Blocking Buffer (Beyotime, P0102) at room temperature for 1
547 hour. Primary antibodies were incubated at room temperature for 1 hour. Coverslips were then
548 washed twice with PBS before incubation with Actin-Tracker Green-488 or second antibodies for
549 1 hour at room temperature. Coverslips were washed twice with PBS before DAPI staining for 10
550 min. Coverslips were washed twice with PBS before mounted in antifade mounting medium.
551 Fluorescent images covering various areas on the coverslips were captured at 12-bit depth in

552 monochrome using a 100x oil immersion objective on the Olympus SpinSR10 confocal
553 microscope and subsequently processed using imageJ software (NIH) with scale bars labeled.

554 **Authentic SARS-CoV-2 Infection of cells**

555 All experiments involving authentic SARS-CoV-2 virus *in vitro* were conducted in the biosafety
556 level 3 (BSL3) laboratory of the Shanghai municipal center for disease control and prevention
557 (CDC). The experiments and protocols in this study were approved by the Ethical Review
558 Committee of the Shanghai CDC. Briefly, HEK293T-ACE2 or Caco-2 cells were seeded into 24-
559 well or 96-well plates at a density of 4 x 10^5 cells per mL overnight, then pre-treated cells with
560 different treatments for 1 hour before infected with 0.5 multiplicity of infection (MOI) Delta or WT
561 authentic SARS-CoV-2 (B.1.617.2 and Wuhan-Hu-1) for 24 hours. Calu-3 cells were seeded into
562 24-well or 96-well plates at a density of 4 x 10^5 cells per mL overnight, infected with 0.5 MOI WT
563 authentic SARS-CoV-2 for 1 hour, then washed with PBS before treated cells with different
564 treatments for 24 hours. Brightfield images were captured to indicate the syncytia formation, cell
565 lysates were collected for spike S2' cleavage and N protein immunoblots.

566 For mice tissue cells, specific pathogen-free 6-week-old female BALB/c mice were lightly
567 anesthetized with isoflurane and intranasal with PBS , mIL-1β (1 μg/kg) or Y-26732 (1 mg/kg) +
568 mIL-1β (1 μg/kg) at day 0, then mice were Intraperitoneal injection with PBS , mIL-1β (1 μg/kg) or
569 Y-26732 (1 mg/kg) + mIL-1β (1 μg/kg) at day 1 and 2. At day 7, mice were anesthetized by
570 intraperitoneal injection of Avertin (2,2,2-tribromoethanol, Sigma-Aldrich), then the thoracic cavity
571 and abdominal cavity of the mice were opened, an outlet was cut in the left ventricle of the mice,
572 and then the right ventricle of the mice was perfused with phosphate buffer saline (PBS) through
573 the pulmonary artery to remove blood cells in the lung. Next, the lung digestive solution with
574 HBSS 1ml, 1 mg/ml collagenase IA, DnaseI (200 mg/ml; Roche), DispaseII (4 U/ml; Gibco) and
575 5% FBS was injected into the lung cavity; and the intestine digestive solution containing DMEM
576 10mL, 1 μM DTT, 0.25 μM EDTA and 5% FBS, then peeled off the lung or intestine organs, and
577 digested for 30 min with shaking at 37°C. After digestion, the cells were resuspended in DMEM
578 supplemented with 10% FBS and 1% P/S, subsequently infected cells with 1 MOI authentic
579 SARS-CoV-2 B.1.351 or BF.7 for 24 hours. All procedures were conducted in compliance with a
580 protocol approved by the Institutional Animal Care and Use Committee (IACUC) at Shanghai
581 Institute of Immunity and Infection, Chinese Academy of Sciences.

582 For human lung cells, the human lung tissues were cut into small pieces of about 2mm and
583 washed three times with HBSS solution containing 1% PS, digested with collagenase type I (100
584 mg+50 mL PBS) in an incubator at 37°C for 4 hours. Then filtered through a 70 μm filter and
585 centrifuged at 500 g for 5 min at room temperature. Lysed with 3 mL Red Blood Cell Lysis Buffer
586 for 5min at room temperature, and then centrifuged at 500 g for 5 min at room temperature,
587 washed twice with HBSS solution containing 1% PS. Human lung cells were resuspended in B-
588 ALI Growth Media and seeded into 96-well plates at a density of 4 x 10^5 cells per mL overnight,
589 infected with 0.5 MOI WT authentic SARS-CoV-2 for 1 hour, then washed with PBS before
590 treated cells with different treatments for 24 hours. The experiments and protocols were approved
591 by the Ethical Review Committee of the Shanghai CDC.

592 **Authentic SARS-CoV-2 infection of BALB/c mice**

593 Specific pathogen-free 6-week-old female BALB/c mice were lightly anesthetized with isoflurane
594 and intranasal with PBS, mIL-1β (1 μg/kg) or mIL-1RA (150 μg/kg) + mIL-1β (1 μg/kg) for 1 hour,
595 then intranasal challenge with 5 × 10^4 FFU of SARS-CoV-2 B.1.351. For booster injection, mice
596 were Intraperitoneal injection with PBS, mIL-1β (1 μg/kg) or mIL-1RA (150 μg/kg) + mIL-1β (1
597 μg/kg) at 1- and 2-days post infection (dpi). Mice were monitored daily for weight loss. Lungs
598 were removed into trizol or 4％PFA at 4 dpi. All protocols were approved by the Institutional
599 Animal Care and Use Committee of the Guangzhou Medical University.

600 **Pulmonary histopathology**

601 Lungs were collected from mice infected by SARS-CoV-2 at 4 dpi and fixed in 4% PFA (Bioss) for
602 12 hours followed by dehydrating, embedded in paraffin for sectioning, then stained with
603 hematoxylin and eosin (H&E), immunohistochemistry (IHC) or immunofluorescence (IF). H&E and
604 IHC analyzed by PerkinElmer Vectra 3, IF analyzed by Olympus SpinSR10 confocal microscope.
605 The pathological scores were judged according to this paper (Curtis, Warnock, Arraj, & Kaltreider,
606 1990).

607 **Statistics analysis**

608 Bar graphs were presented as mean values ± standard error of mean (SEM) with individual data
609 points. All statistical analyses were carried out with the Prism software v8.0.2 (GraphPad). Data
610 with multiple groups were analyzed using matched one-way ANOVA followed by Sidak's post hoc
611 comparisons. Statistical significance P values were indicated between compared groups and
612 shown on Figures.
613
614
615 **Acknowledgments**
616
617 We thank Qiuhong Guo, Prof. Dimitri Lavillette and Prof. Gary Wong for their experimental
618 supports and key reagents used in this work. This study is supported by grants from Natural
619 Science Foundation of China (92269202, 82825001, 92054104), National Key R&D Program of
620 China (2022YFC2304700, 2022YFC2303200, 2022YFC2303502), Three-Year Initiative Plan for
621 Strengthening Public Health System Construction in Shanghai (2023-2025) Key Discipline Project
622 (GWVI-11.1-09), as well as the Shanghai Municipal Science and Technology Major Project
623 (2019SHZDZX02). Guangdong Basic and Applied Basic Research Foundation
624 (2023A1515010152) and Young Scientists Fund of the Guangzhou National Laboratory
625 (QNPG23-03).
626
627
628 **References**

629 Arabi, Y. M., Mandourah, Y., Al-Hameed, F., Sindi, A. A., Almekhlafi, G. A., Hussein, M. A., . . .
630 Fowler, R. A. (2018). Corticosteroid Therapy for Critically Ill Patients with Middle East
631 Respiratory Syndrome. *Am J Respir Crit Care Med, 197*(6), 757-767. doi:10.1164/rccm.201706-
632 1172OC
633 Barnett, K. C., Xie, Y., Asakura, T., Song, D., Liang, K., Taft-Benz, S. A., . . . Ting, J. P. (2023). An
634 epithelial-immune circuit amplifies inflammasome and IL-6 responses to SARS-CoV-2. Cell Host
635 Microbe, 31(2), 243-259 e246. doi:10.1016/j.chom.2022.12.005
636 Belouzard, S., Chu, V. C., & Whittaker, G. R. (2009). Activation of the SARS coronavirus spike
637 protein via sequential proteolytic cleavage at two distinct sites. Proc Natl Acad Sci U S A,
638 106(14), 5871-5876. doi:10.1073/pnas.0809524106
639 Blanco-Melo, D., Nilsson-Payant, B. E., Liu, W. C., Uhl, S., Hoagland, D., Møller, R., . . . tenOever,
640 B. R. (2020). Imbalanced Host Response to SARS-CoV-2 Drives Development of COVID-19. Cell,
641 181(5), 1036-1045 e1039. doi:10.1016/j.cell.2020.04.026
642 Bussani, R., Schneider, E., Zentilin, L., Collesi, C., Ali, H., Braga, L., . . . Giacca, M. (2020).
643 Persistence of viral RNA, pneumocyte syncytia and thrombosis are hallmarks of advanced
644 COVID-19 pathology. *EBioMedicine, 61*, 103104. doi:10.1016/j.ebiom.2020.103104
645 Cavalli, G., De Luca, G., Campochiaro, C., Della-Torre, E., Ripa, M., Canetti, D., . . . Dagna, L.
646 (2020). Interleukin-1 blockade with high-dose anakinra in patients with COVID-19, acute

respiratory distress syndrome, and hyperinflammation: a retrospective cohort study. *Lancet Rheumatol, 2*(6), e325-e331. doi:10.1016/s2665-9913(20)30127-2

Chen, L. Y., Zuraw, B. L., Liu, F. T., Huang, S., & Pan, Z. K. (2002). IL-1 receptor-associated kinase and low molecular weight GTPase RhoA signal molecules are required for bacterial lipopolysaccharide-induced cytokine gene transcription. *J Immunol, 169*(7), 3934-3939. doi:10.4049/jimmunol.169.7.3934

Curtis, J. L., Warnock, M. L., Arraj, S. M., & Kaltreider, H. B. (1990). Histologic analysis of an immune response in the lung parenchyma of mice. Angiopathy accompanies inflammatory cell influx. *Am J Pathol, 137*(3), 689-699.

Delespaul, L., Gélabert, C., Lesluyes, T., Le Guellec, S., Pérot, G., Leroy, L., . . . Chibon, F. (2020). Cell-cell fusion of mesenchymal cells with distinct differentiations triggers genomic and transcriptomic remodelling toward tumour aggressiveness. *Sci Rep, 10*(1), 21634. doi:10.1038/s41598-020-78502-z

Della-Torre, E., Criscuolo, E., Lanzillotta, M., Locatelli, M., Clementi, N., Mancini, N., & Dagna, L. (2021). IL-1 and IL-6 inhibition affects the neutralising activity of anti-SARS-CoV-2 antibodies in patients with COVID-19. *Lancet Rheumatol, 3*(12), e829-e831. doi:10.1016/s2665-9913(21)00321-0

Di Paolo, N. C., Miao, E. A., Iwakura, Y., Murali-Krishna, K., Aderem, A., Flavell, R. A., . . . Shayakhmetov, D. M. (2009). Virus binding to a plasma membrane receptor triggers interleukin-1 alpha-mediated proinflammatory macrophage response in vivo. *Immunity, 31*(1), 110-121. doi:10.1016/j.immuni.2009.04.015

Doherty, J. T., Lenhart, K. C., Cameron, M. V., Mack, C. P., Conlon, F. L., & Taylor, J. M. (2011). Skeletal muscle differentiation and fusion are regulated by the BAR-containing Rho-GTPase-activating protein (Rho-GAP), GRAF1. *J Biol Chem, 286*(29), 25903-25921. doi:10.1074/jbc.M111.243030

Dupraz, S., Hilton, B. J., Husch, A., Santos, T. E., Coles, C. H., Stern, S., . . . Bradke, F. (2019). RhoA Controls Axon Extension Independent of Specification in the Developing Brain. *Curr Biol, 29*(22), 3874-3886 e3879. doi:10.1016/j.cub.2019.09.040

Eisenbarth, S. C., Colegio, O. R., O'Connor, W., Sutterwala, F. S., & Flavell, R. A. (2008). Crucial role for the Nalp3 inflammasome in the immunostimulatory properties of aluminium adjuvants. *Nature, 453*(7198), 1122-1126. doi:10.1038/nature06939

García-García, A., Pérez de Diego, R., Flores, C., Rinchai, D., Solé-Violán, J., Deyà-Martínez, À., . . . Rodríguez-Gallego, C. (2023). Humans with inherited MyD88 and IRAK-4 deficiencies are predisposed to hypoxemic COVID-19 pneumonia. *J Exp Med, 220*(5). doi:10.1084/jem.20220170

Hadjadj, J., Yatim, N., Barnabei, L., Corneau, A., Boussier, J., Smith, N., . . . Terrier, B. (2020). Impaired type I interferon activity and inflammatory responses in severe COVID-19 patients. *Science, 369*(6504), 718-724. doi:10.1126/science.abc6027

Han, X., Alameh, M. G., Butowska, K., Knox, J. J., Lundgreen, K., Ghattas, M., . . . Mitchell, M. J. (2023). Adjuvant lipidoid-substituted lipid nanoparticles augment the immunogenicity of SARS-CoV-2 mRNA vaccines. *Nat Nanotechnol*. doi:10.1038/s41565-023-01404-4

Hilligan, K. L., Namasivayam, S., Clancy, C. S., O'Mard, D., Oland, S. D., Robertson, S. J., . . . Sher, A. (2022). Intravenous administration of BCG protects mice against lethal SARS-CoV-2 challenge. *J Exp Med, 219*(2). doi:10.1084/jem.20211862

Huet, T., Beaussier, H., Voisin, O., Jouveshomme, S., Dauriat, G., Lazareth, I., . . . Hayem, G. (2020). Anakinra for severe forms of COVID-19: a cohort study. *Lancet Rheumatol, 2*(7), e393-e400. doi:10.1016/s2665-9913(20)30164-8

Karki, R., Sharma, B. R., Tuladhar, S., Williams, E. P., Zalduondo, L., Samir, P., . . . Kanneganti, T. D. (2021). Synergism of TNF-α and IFN-γ Triggers Inflammatory Cell Death, Tissue Damage, and Mortality in SARS-CoV-2 Infection and Cytokine Shock Syndromes. *Cell, 184*(1), 149-168 e117. doi:10.1016/j.cell.2020.11.025

Lee, A., Floyd, K., Wu, S., Fang, Z., Tan, T. K., Froggatt, H. M., . . . Pulendran, B. (2023). BCG vaccination stimulates integrated organ immunity by feedback of the adaptive immune response to imprint prolonged innate antiviral resistance. *Nat Immunol*. doi:10.1038/s41590-023-01700-0

Lee, N., Allen Chan, K. C., Hui, D. S., Ng, E. K., Wu, A., Chiu, R. W., . . . Lo, Y. M. (2004). Effects of early corticosteroid treatment on plasma SARS-associated Coronavirus RNA concentrations in adult patients. *J Clin Virol, 31*(4), 304-309. doi:10.1016/j.jcv.2004.07.006

Li, Z., Li, S., Zhang, G., Peng, W., Chang, Z., Zhang, X., . . . Wu, Y. (2022). An engineered bispecific human monoclonal antibody against SARS-CoV-2. *Nat Immunol, 23*(3), 423-430. doi:10.1038/s41590-022-01138-w

Martínez-Mármol, R., Giordano-Santini, R., Kaulich, E., Cho, A. N., Przybyla, M., Riyadh, M. A., . . . Hilliard, M. A. (2023). SARS-CoV-2 infection and viral fusogens cause neuronal and glial fusion that compromises neuronal activity. *Sci Adv, 9*(23), eadg2248. doi:10.1126/sciadv.adg2248

Medzhitov, R. (2001). Toll-like receptors and innate immunity. *Nat Rev Immunol, 1*(2), 135-145. doi:10.1038/35100529

Nishiyama, T., Kii, I., & Kudo, A. (2004). Inactivation of Rho/ROCK signaling is crucial for the nuclear accumulation of FKHR and myoblast fusion. *J Biol Chem, 279*(45), 47311-47319. doi:10.1074/jbc.M403546200

Nobes, C. D., & Hall, A. (1999). Rho GTPases control polarity, protrusion, and adhesion during cell movement. *J Cell Biol, 144*(6), 1235-1244. doi:10.1083/jcb.144.6.1235

Pfaender, S., Mar, K. B., Michailidis, E., Kratzel, A., Boys, I. N., V'Kovski, P., . . . Thiel, V. (2020). LY6E impairs coronavirus fusion and confers immune control of viral disease. *Nat Microbiol, 5*(11), 1330-1339. doi:10.1038/s41564-020-0769-y

Powell, A. E., Anderson, E. C., Davies, P. S., Silk, A. D., Pelz, C., Impey, S., & Wong, M. H. (2011). Fusion between Intestinal epithelial cells and macrophages in a cancer context results in nuclear reprogramming. *Cancer Res, 71*(4), 1497-1505. doi:10.1158/0008-5472.can-10-3223

Priya, R., Gomez, G. A., Budnar, S., Verma, S., Cox, H. L., Hamilton, N. A., & Yap, A. S. (2015). Feedback regulation through myosin II confers robustness on RhoA signalling at E-cadherin junctions. *Nat Cell Biol, 17*(10), 1282-1293. doi:10.1038/ncb3239

Rajah, M. M., Bernier, A., Buchrieser, J., & Schwartz, O. (2022). The Mechanism and Consequences of SARS-CoV-2 Spike-Mediated Fusion and Syncytia Formation. *J Mol Biol, 434*(6), 167280. doi:10.1016/j.jmb.2021.167280

Ren, X., Wen, W., Fan, X., Hou, W., Su, B., Cai, P., . . . Zhang, Z. (2021). COVID-19 immune features revealed by a large-scale single-cell transcriptome atlas. *Cell, 184*(7), 1895-1913 e1819. doi:10.1016/j.cell.2021.01.053

Riento, K., & Ridley, A. J. (2003). Rocks: multifunctional kinases in cell behaviour. *Nat Rev Mol Cell Biol, 4*(6), 446-456. doi:10.1038/nrm1128

Rivas, M. N., Ebinger, J. E., Wu, M., Sun, N., Braun, J., Sobhani, K., . . . Arditi, M. (2021). BCG vaccination history associates with decreased SARS-CoV-2 seroprevalence across a diverse cohort of health care workers. *J Clin Invest, 131*(2). doi:10.1172/jci145157

Rodríguez-Pérez, F., Manford, A. G., Pogson, A., Ingersoll, A. J., Martínez-González, B., & Rape, M. (2021). Ubiquitin-dependent remodeling of the actin cytoskeleton drives cell fusion. *Dev Cell, 56*(5), 588-601 e589. doi:10.1016/j.devcel.2021.01.016

740 Sefik, E., Qu, R., Junqueira, C., Kaffe, E., Mirza, H., Zhao, J., . . . Flavell, R. A. (2022).
741 Inflammasome activation in infected macrophages drives COVID-19 pathology. *Nature,*
742 *606*(7914), 585-593. doi:10.1038/s41586-022-04802-1
743 Stern, S., Hilton, B. J., Burnside, E. R., Dupraz, S., Handley, E. E., Gonyer, J. M., . . . Bradke, F.
744 (2021). RhoA drives actin compaction to restrict axon regeneration and astrocyte reactivity after
745 CNS injury. *Neuron, 109*(21), 3436-3455 e3439. doi:10.1016/j.neuron.2021.08.014
746 Straus, M. R., Tang, T., Lai, A. L., Flegel, A., Bidon, M., Freed, J. H., . . . Whittaker, G. R. (2020).
747 Ca(2+) Ions Promote Fusion of Middle East Respiratory Syndrome Coronavirus with Host Cells
748 and Increase Infectivity. *J Virol, 94*(13). doi:10.1128/jvi.00426-20
749 Sun, L., Guan, R., Lee, I. J., Liu, Y., Chen, M., Wang, J., . . . Chen, Z. (2015). Mechanistic insights
750 into the anchorage of the contractile ring by anillin and Mid1. *Dev Cell, 33*(4), 413-426.
751 doi:10.1016/j.devcel.2015.03.003
752 Tahtinen, S., Tong, A. J., Himmels, P., Oh, J., Paler-Martinez, A., Kim, L., . . . Mellman, I. (2022). IL-
753 1 and IL-1ra are key regulators of the inflammatory response to RNA vaccines. *Nat Immunol,*
754 *23*(4), 532-542. doi:10.1038/s41590-022-01160-y
755 Tharaux, P.-L., Pialoux, G., Pavot, A., Mariette, X., Hermine, O., Resche-Rigon, M., . . . Renet, S.
756 (2021). Effect of anakinra versus usual care in adults in hospital with COVID-19 and mild-to-
757 moderate pneumonia (CORIMUNO-ANA-1): a randomised controlled trial. *The Lancet*
758 *Respiratory Medicine, 9*(3), 295-304. doi:https://doi.org/10.1016/S2213-2600(20)30556-7
759 Ucciferri, C., Auricchio, A., Di Nicola, M., Potere, N., Abbate, A., Cipollone, F., . . . Falasca, K.
760 (2020). Canakinumab in a subgroup of patients with COVID-19. *Lancet Rheumatol, 2*(8), e457-
761 ee458. doi:10.1016/s2665-9913(20)30167-3
762 van der Heijden, M., Versteilen, A. M., Sipkema, P., van Nieuw Amerongen, G. P., Musters, R. J.,
763 & Groeneveld, A. B. (2008). Rho-kinase-dependent F-actin rearrangement is involved in the
764 inhibition of PI3-kinase/Akt during ischemia-reperfusion-induced endothelial cell apoptosis.
765 *Apoptosis, 13*(3), 404-412. doi:10.1007/s10495-007-0173-6
766 Wang, S., Li, W., Hui, H., Tiwari, S. K., Zhang, Q., Croker, B. A., . . . Rana, T. M. (2020). Cholesterol
767 25-Hydroxylase inhibits SARS-CoV-2 and other coronaviruses by depleting membrane
768 cholesterol. *EMBO J, 39*(21), e106057. doi:10.15252/embj.2020106057
769 Watanabe, N., Kato, T., Fujita, A., Ishizaki, T., & Narumiya, S. (1999). Cooperation between
770 mDia1 and ROCK in Rho-induced actin reorganization. *Nat Cell Biol, 1*(3), 136-143.
771 doi:10.1038/11056
772 Weber, A., Wasiliew, P., & Kracht, M. (2010). Interleukin-1beta (IL-1beta) processing pathway.
773 *Sci Signal, 3*(105), cm2. doi:10.1126/scisignal.3105cm2
774 Xiao, N., Nie, M., Pang, H., Wang, B., Hu, J., Meng, X., . . . Hu, Z. (2021). Integrated cytokine and
775 metabolite analysis reveals immunometabolic reprogramming in COVID-19 patients with
776 therapeutic implications. *Nat Commun, 12*(1), 1618. doi:10.1038/s41467-021-21907-9
777 Yu, S., Zheng, X., Zhou, B., Li, J., Chen, M., Deng, R., . . . Meng, G. (2022). SARS-CoV-2 spike
778 engagement of ACE2 primes S2' site cleavage and fusion initiation. *Proc Natl Acad Sci U S A,*
779 *119*(1). doi:10.1073/pnas.2111199119
780 Yu, S., Zheng, X., Zhou, Y., Gao, Y., Zhou, B., Zhao, Y., . . . Meng, G. (2023). Antibody-mediated
781 spike activation promotes cell-cell transmission of SARS-CoV-2. *PLoS Pathog, 19*(11), e1011789.
782 doi:10.1371/journal.ppat.1011789
783 Zhou, P., Yang, X. L., Wang, X. G., Hu, B., Zhang, L., Zhang, W., . . . Shi, Z. L. (2020). A pneumonia
784 outbreak associated with a new coronavirus of probable bat origin. *Nature, 579*(7798), 270-273.
785 doi:10.1038/s41586-020-2012-7

Figures

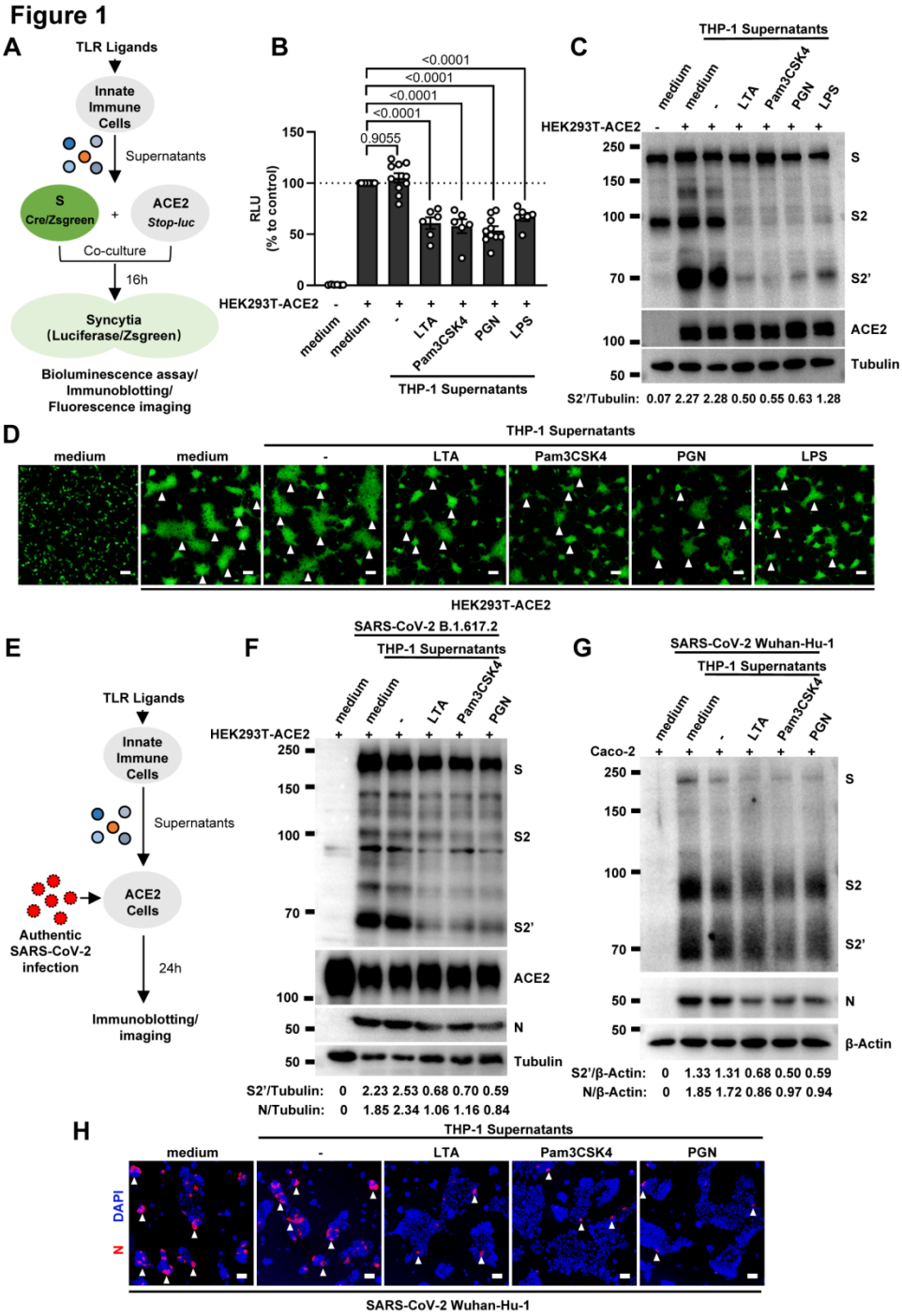

Fig. 1. Host factors secreted by activated innate immune cells inhibit SARS-CoV-2 induced cell-cell fusion.

(**A**) Schematics of the cell-cell fusion model used to quantify spike-mediated syncytium formation upon treatment with cell culture supernatants from TLR ligands stimulated innate immune cells. Cells co-expressing SARS-CoV-2 spike and Cre, were co-cultured with ACE2 and *Stop-luc* co-expressing HEK293T cells for 16 hours, before cell lysates were collected for bioluminescence

795 assay and immunoblotting. Cells co-expressing SARS-CoV-2 spike and Zsgreen, were co-
796 cultured with ACE2 expressing HEK293T cells for 16 hours before fluorescence imaging. (**B**)
797 Luciferase activity (RLU) measured from HEK293T cell lysates collected from THP-1
798 supernatants treated HEK293T-S and HEK293T-ACE2 described in (A) for 16 hours. FBS free
799 RPMI 1640 served as medium control group. Data are representative of six individual repeats and
800 displayed as individual points with mean ± standard error of the mean (SEM). (**C**) Immunoblots
801 showing full-length spike, S2, cleaved S2' and ACE2 collected from THP-1 supernatants treated
802 HEK293T-S and HEK293T-ACE2 described in (A) for 16 hours. Blots are representative of three
803 independent experiments. Numbers below the blots indicated the ratio of S2' versus Tubulin. (**D**)
804 Representative fluorescent image captured at 488 nm from THP-1 supernatants treated
805 HEK293T-S-Zsgreen and HEK293T-ACE2 for 16 hours. (**E**) Schematic presentation of THP-1
806 supernatants pre-treatment on authentic SARS-CoV-2 infected cells. Pre-treatment of HEK293T-
807 ACE2 cells with THP-1 supernatants for 1 hour, then inoculated with 0.5 multiplicity of infection
808 (MOI) Delta or WT authentic SARS-CoV-2 (B.1.617.2 and Wuhan-Hu-1) virus. Imaging was
809 performed at 24 hours post-infection (hpi) before cell lysates were harvested for immunoblotting.
810 (**F**) Immunoblots of Delta SARS-CoV-2 S, S2, cleaved S2', N and ACE2 proteins collected from
811 HEK293T-ACE2 cells 24 hpi as described in (E). Blots are representative of three individual
812 experiments. Numbers below the blots indicated the ratio of S2' or N versus Tubulin. (**G**)
813 Immunoblots of WT SARS-CoV-2 S, S2, cleaved S2' and N proteins collected from Caco-2 cells
814 24 hpi as described in (E). Blots are representative of three individual experiments. Numbers
815 below the blots indicated the ratio of S2' or N versus β-Actin. (**H**) Immunofluorescent images
816 showing morphology of SARS-CoV-2 infected Caco-2 cells pre-treated with THP-1 supernatants.
817 Anti-SARS-CoV-2 N was stained with Alexa fluor 555 and nuclei were counterstained with DAPI
818 respectively. White arrow heads in (D and H) indicate syncytia formation or infected cells, scale
819 bars are indicative of 50 μm and images are representative of three independent experiments.

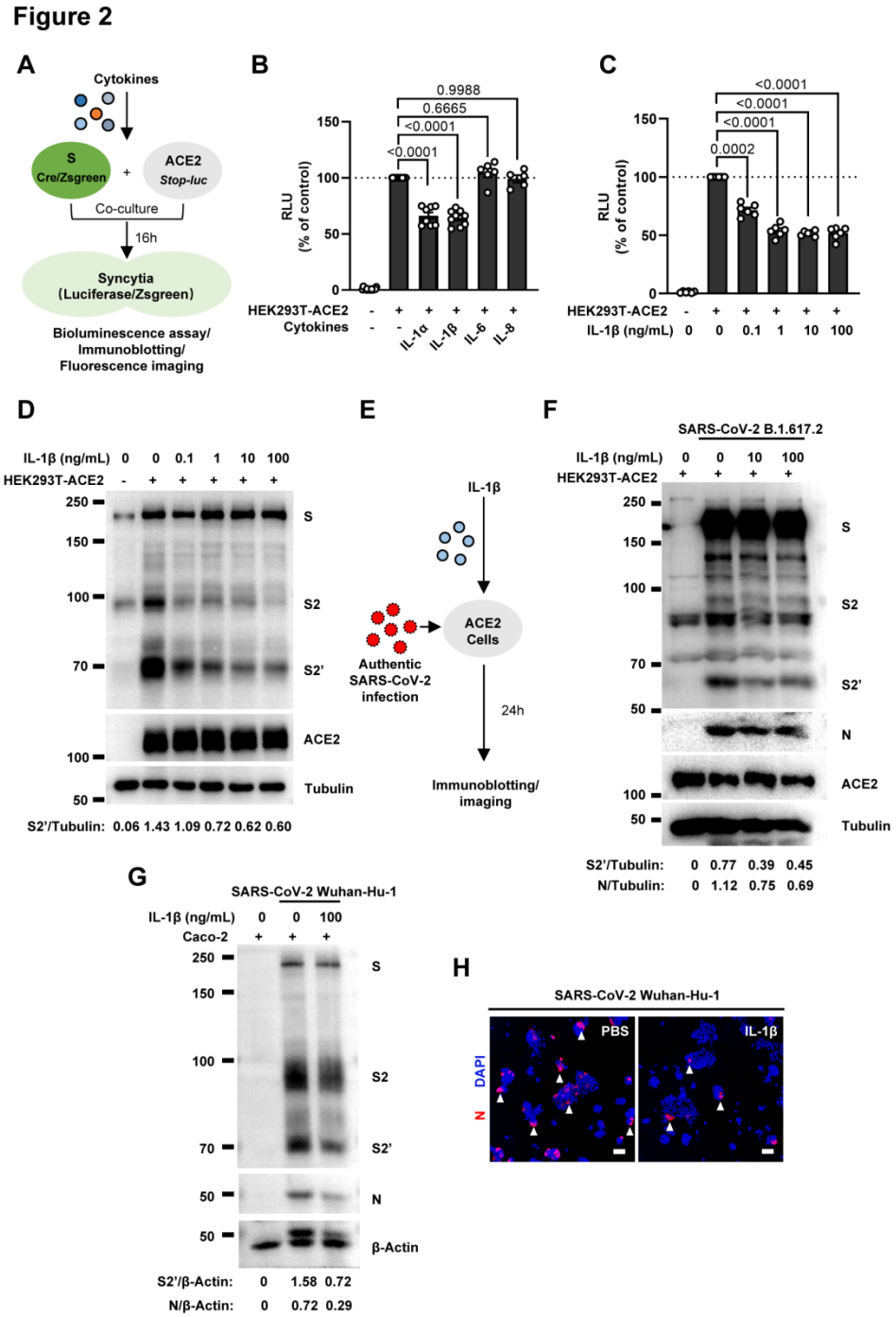

Fig. 2. IL-1β inhibits SARS-CoV-2 induced cell-cell fusion.

(**A**) Schematics of the cell-cell fusion model used to quantify spike-mediated syncytium formation upon treatment with different cytokines. Cells co-expressing SARS-CoV-2 spike and Cre, were co-cultured with ACE2 and *Stop-luc* co-expressing HEK293T cells for 16 hours, before cell lysates were collected for bioluminescence assay and immunoblotting. Cells co-expressing SARS-CoV-2 spike and Zsgreen, were co-cultured with ACE2 expressing HEK293T cells for 16 hours before fluorescence imaging. (**B**) Luciferase activity (RLU) measured from HEK293T cell lysates collected from different cytokines treated HEK293T-S and HEK293T-ACE2 described in

829 (A) for 16 hours. IL-1α (10 ng/mL), IL-1β (1 ng/mL), IL-6 (100 ng/mL) or IL-8 (100 ng/mL) were
830 added into the cell-cell fusion system. Data are representative of six individual repeats and
831 displayed as individual points with mean ± standard error of the mean (SEM). (**C**) Luciferase
832 activity (RLU) measured from HEK293T cell lysates collected from different concentrations of IL-
833 1β treated HEK293T-S and HEK293T-ACE2 for 16 hours. Data are representative of six
834 individual repeats and displayed as individual points with mean ± standard error of the mean
835 (SEM). (**D**) Immunoblots showing full-length spike, S2, cleaved S2' and ACE2 collected from
836 different concentrations of IL-1β treated HEK293T-S and HEK293T-ACE2 for 16 hours. Blots are
837 representative of three independent experiments. Numbers below the blots indicated the ratio of
838 S2' versus Tubulin. (**E**) Schematic presentation of IL-1β pre-treatment on authentic SARS-CoV-2
839 infected cells. Pre-treatment of HEK293T-ACE2 cells with different concentrations of IL-1β for 1
840 hour, then inoculated with 0.5 MOI Delta or WT authentic SARS-CoV-2 (B.1.617.2 and Wuhan-
841 Hu-1) virus. Brightfield images were captured at 24 hours post-infection (hpi) before cell lysates
842 were harvested for immunoblotting. (**F**) Immunoblots of Delta SARS-CoV-2 S, S2, cleaved S2', N
843 and ACE2 proteins collected from HEK293T-ACE2 cells 24 hpi as described in (E). Blots are
844 representative of three individual experiments. Numbers below the blots indicated the ratio of S2'
845 or N versus Tubulin. (**G**) Immunoblots of WT SARS-CoV-2 S, S2, cleaved S2' and N proteins
846 collected from Caco-2 cells 24 hpi as described in (E). Blots are representative of three individual
847 experiments. Numbers below the blots indicated the ratio of S2' or N versus β-Actin. (**H**)
848 Immunofluorescent images showing morphology of SARS-CoV-2 infected Caco-2 cells pre-
849 treated with or without IL-1β. Anti-SARS-CoV-2 N was stained with Alexa fluor 555 and nuclei
850 were counterstained with DAPI respectively. White arrow heads indicate syncytia formation or
851 infected cells, scale bars are indicative of 50 μm and images are representative of three
852 independent experiments.

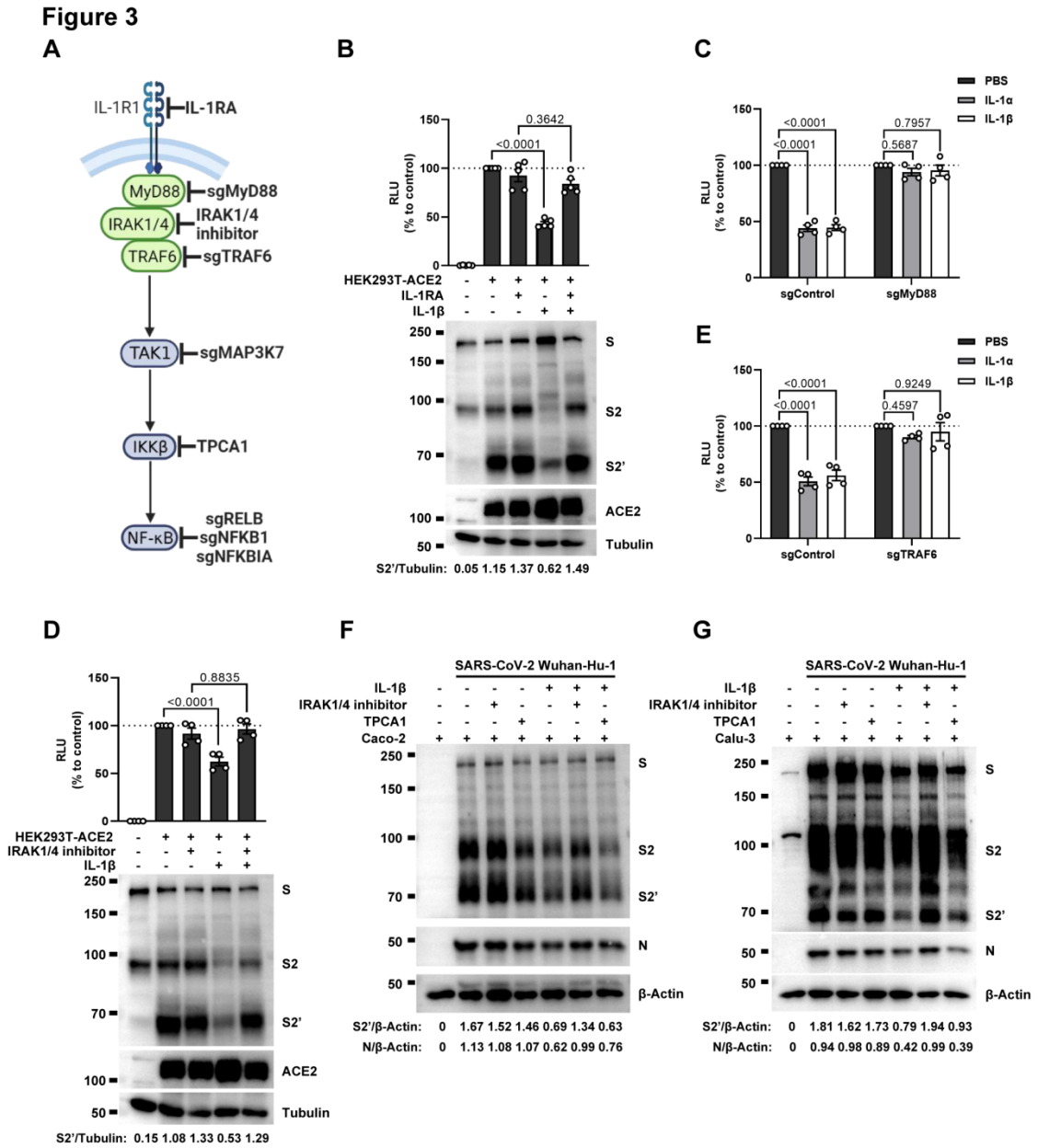

Fig. 3. IL-1β inhibits SARS-CoV-2 induced cell-cell fusion through IL-1R1/MyD88/IRAK/TRAF6 pathway.

(**A**) Schematics of gene knockout or inhibitor treatment in the IL-1 receptor pathway. (**B**) Luciferase activity (RLU) measured from HEK293T cell lysates and immunoblots showing full-length spike, S2, cleaved S2' and ACE2 collected from HEK293T-S and HEK293T-ACE2 pre-treated with 1000 ng/mL IL-1RA for 30 min, then treated with 1 ng/mL IL-1β for 16 hours. Data and blots are representative of five individual repeats. Numbers below the blots indicated the ratio of S2' versus Tubulin. (**C**) Luciferase activity (RLU) measured from cell lysates collected from 10 ng/mL IL-1α or 1 ng/mL IL-1β treated sgControl or sgMyD88 HEK293T cell-cell fusion system for 16 hours. Data are representative of four individual repeats and displayed as individual points with mean ± standard error of the mean (SEM). (**D**) Luciferase activity (RLU) measured from HEK293T cell lysates and immunoblots showing full-length spike, S2, cleaved S2' and ACE2

866 collected from HEK293T-S and HEK293T-ACE2 pre-treated with 2μM IRAK1/4 inhibitor for 30
867 min, then treated with 1 ng/mL IL-1β for 16 hours. Data and blots are representative of four
868 individual repeats. Numbers below the blots indicated the ratio of S2' versus Tubulin. (**E**)
869 Luciferase activity (RLU) measured from cell lysates collected from 10 ng/mL IL-1α or 1 ng/mL IL-
870 1β treated sgControl or sgTRAF6 HEK293T cell-cell fusion system for 16 hours. Data are
871 representative of four individual repeats and displayed as individual points with mean ± standard
872 error of the mean (SEM). (**F**) Immunoblots showing full-length spike, S2, cleaved S2' and ACE2
873 collected from Caco-2 cells, which pre-treated with 2μM IRAK1/4 inhibitor and 10 ng/mL IL-1β for
874 1 hour, then infected with authentic SARS-CoV-2 for 24 hours. Blots are representative of three
875 independent experiments. Numbers below the blots indicated the ratio of S2' or N versus β-Actin.
876 (**G**) Immunoblots showing full-length spike, S2, cleaved S2' and ACE2 collected from Calu-3
877 cells, which infected with authentic SARS-CoV-2 for 1 hour, then washed with PBS before treated
878 with 2μM IRAK1/4 inhibitor and 10 ng/mL IL-1β for 24 hours. Blots are representative of three
879 independent experiments. Numbers below the blots indicated the ratio of S2' or N versus β-Actin.

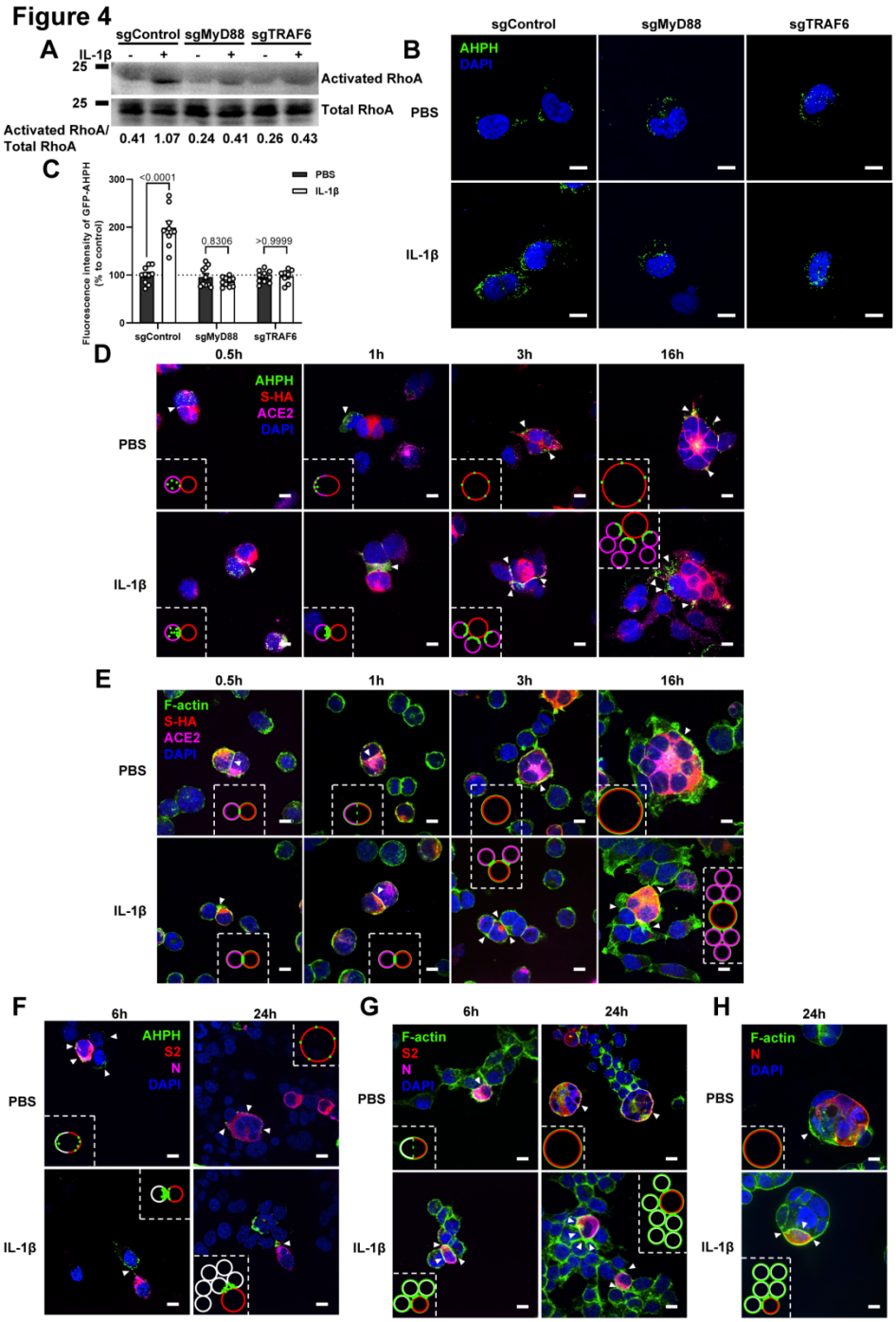

Fig. 4. IL-1β inhibits SARS-CoV-2 induced cell-cell fusion through RhoA/ROCK mediated actin bundles at cell-cell junction.

(**A**) GTP-RhoA pull-down assay to detect the active level of RhoA in sgControl, sgMyD88 and sgTRAF6 HEK293T cells after 1 ng/mL IL-1β treatment for 30 min. Immunoblots showing activated RhoA and total RhoA. Blots are representative of three independent experiments. Numbers below the blots indicated the ratio of active RhoA versus total RhoA. (**B**) Representative confocal images of GFP-AHPH after 1 ng/mL IL-1β treatment for 30 min in sgControl, sgMyD88 and sgTRAF6 HEK293T cells. Scale bars, 10 μm. (**C**) Quantification of fluorescence intensity of

889 GFP-AHPH in (B). Data are representative of eight individual repeats. (**D**) Representative
890 confocal images of GFP-AHPH localization with or without 1 ng/mL IL-1β treatment at different
891 time points of syncytia formation in HEK293T-S-HA and HEK293T-ACE2 cells. Schematics with
892 green dots in the white dashed line boxes representing GFP-AHPH, red cycles representing S-
893 expressing cells, and magenta cycles representing ACE2-expressing cells. White arrow heads
894 indicate the localization of GFP-AHPH, scale bars, 10 μm. Images are representative of three
895 independent experiments. (**E**) Representative confocal images of F-actin stained with phalloidin-
896 488 in the presence or absence of 1 ng/mL IL-1β treatment at different time points of syncytia
897 formation in HEK293T-S-HA and HEK293T-ACE2 cells. Schematics with green lines in the white
898 dashed line boxes representing actin bundles, red cycles representing S-expressing cells, and
899 magenta cycles representing ACE2-expressing cells. White arrow heads indicate the enrichment
900 or disappearance of F-actin, scale bars, 10 μm. Images are representative of three independent
901 experiments. (**F**) Representative confocal images of GFP-AHPH localization with or without 1
902 ng/mL IL-1β treatment in 0.5 MOI WT authentic SARS-CoV-2 infected HEK293T-ACE2 cells at 6
903 hpi and 24 hpi. Schematics with green dots in the white dashed line boxes representing GFP-
904 AHPH, red cycles representing SARS-CoV-2 infected cells, and white cycles representing
905 neighboring cells. White arrow heads indicate the localization of GFP-AHPH, scale bars, 10 μm.
906 Images are representative of three independent experiments. (**G, H**) Representative confocal
907 images of F-actin stained with phalloidin-488 in the presence or absence of 1 ng/mL IL-1β
908 treatment in 0.5 MOI WT authentic SARS-CoV-2 infected HEK293T-ACE2 cells at 6 hpi and 24
909 hpi (**G**) or Caco-2 cells at 24 hpi (**H**). Schematics with green lines in the white dashed line boxes
910 representing actin bundles, red cycles representing SARS-CoV-2 infected cells, and white cycles
911 representing neighboring cells. Scale bars, 10 μm. Images are representative of three
912 independent experiments. White arrow heads in (G and H) indicate the enrichment or
913 disappearance of F-actin.

Figure 5

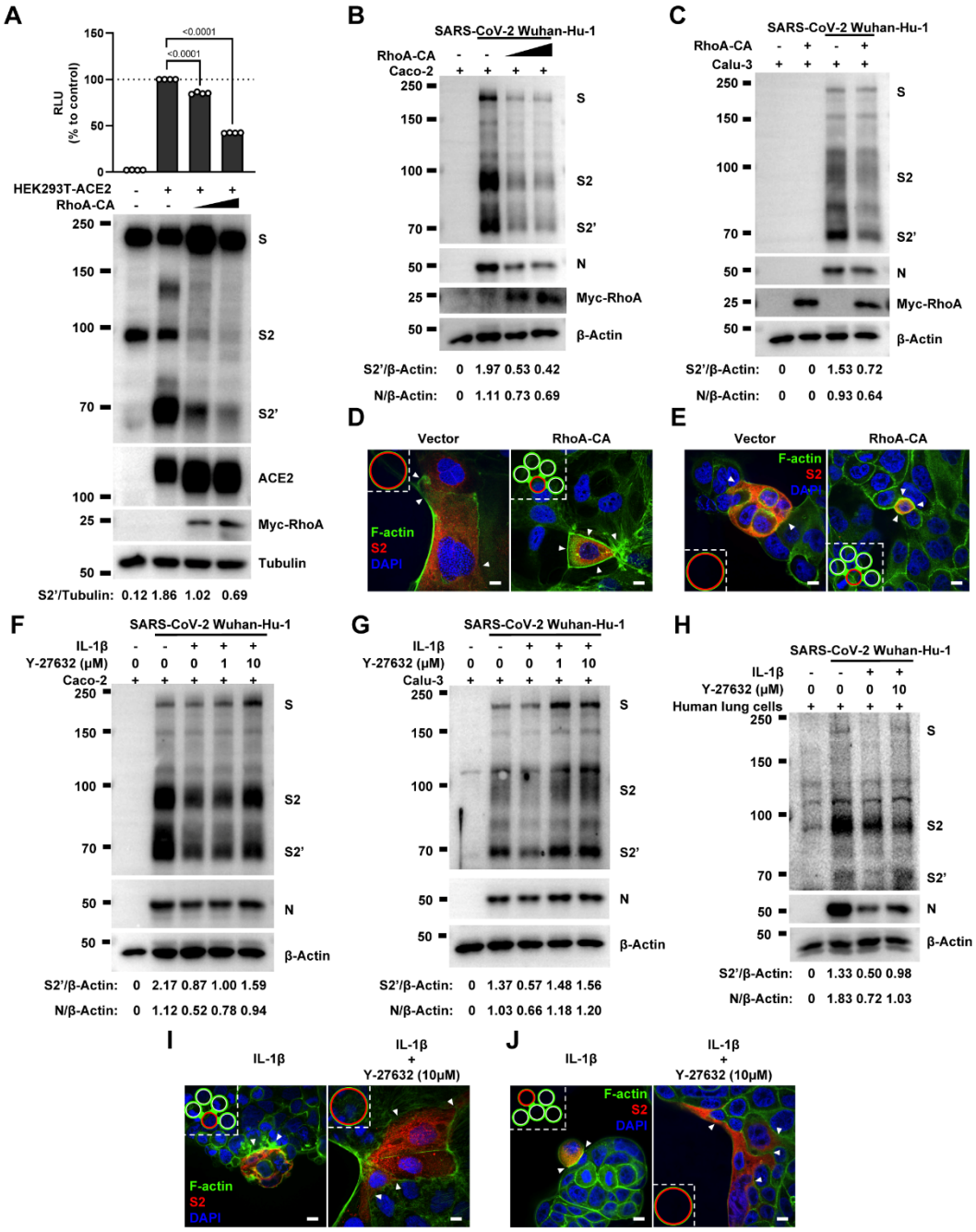

Fig. 5. Activation of RhoA/ROCK pathway prevents authentic SARS-CoV-2 induced cell-cell fusion by forming actin bundles.

(**A**) Luciferase activity (RLU) measured from HEK293T cell lysates and immunoblots showing full-length spike, S2, cleaved S2', ACE2 and Myc-RhoA collected from transfected vector, 10 ng or 20 ng constitutively active RhoA mutant (RhoA-CA) both in HEK293T-S and HEK293T-ACE2. Data and blots are representative of four individual repeats. Numbers below the blots indicated the ratio of S2' versus Tubulin. (**B**) Immunoblots of WT SARS-CoV-2 S, S2, cleaved S2', N and Myc-RhoA collected from Caco-2 cells, which transfected with vector, 10 ng or 20 ng RhoA-CA

923 before infected with 0.5 MOI WT authentic SARS-CoV-2 for 24 hours. Blots are representative of
924 three individual experiments. Numbers below the blots indicated the ratio of S2' or N versus β-
925 Actin. (**C**) Immunoblots of WT SARS-CoV-2 S, S2, cleaved S2', N and Myc-RhoA collected from
926 lentivirus-transduced Calu-3 cells expressing vector or RhoA-CA, infected with WT authentic
927 SARS-CoV-2 for 24 hours. Blots are representative of three individual experiments. Numbers
928 below the blots indicated the ratio of S2' or N versus β-Actin. (**D**) Representative confocal images
929 of F-actin stained with phalloidin-488 from Caco-2 cells described in (B). Schematics with green
930 lines in the white dashed line boxes representing actin bundles, red cycles representing S-
931 expressing cells. Scale bars, 10 μm. Images are representative of four independent experiments.
932 (**E**) Representative confocal images of F-actin stained with phalloidin-488 from Calu-3 cells
933 described in (C). Schematics with green lines in the white dashed line boxes representing actin
934 bundles, red cycles representing S-expressing cells. White arrow heads in (D and E) indicate the
935 enrichment or disappearance of F-actin, scale bars, 10 μm. Images are representative of four
936 independent experiments. (**F**) Immunoblots of WT SARS-CoV-2 S, S2, cleaved S2' and N
937 collected from Caco-2 cells, which treated with different concentrations of Y-27632 and 10 ng/mL
938 IL-1β for 1 hour, then infected with 0.5 MOI WT authentic SARS-CoV-2 for 24 hours. Blots are
939 representative of three individual experiments. Numbers below the blots indicated the ratio of S2'
940 or N versus β-Actin. (**G**) Immunoblots of WT SARS-CoV-2 S, S2, cleaved S2' and N collected
941 from Calu-3 cells, which infected with authentic SARS-CoV-2 for 1 hour, then washed with PBS
942 before treated with different concentrations of Y-27632 and 10 ng/mL IL-1β for 24 hours. Blots
943 are representative of three independent experiments. Numbers below the blots indicated the ratio
944 of S2' or N versus β-Actin. (**H**) Immunoblots of WT SARS-CoV-2 S, S2, cleaved S2' and N
945 collected from human lung cells, which infected with authentic SARS-CoV-2 for 1 hour, then
946 washed with PBS before treated with 10 μM Y-27632 and 10 ng/mL IL-1β for 24 hours. Blots are
947 representative of three independent experiments. Numbers below the blots indicated the ratio of
948 S2' or N versus β-Actin. (**I**) Representative confocal images of F-actin stained with phalloidin-488
949 in Caco-2 cells described in (G). Schematics with green lines in the white dashed line boxes
950 representing actin bundles, red cycles representing S-expressing cells. Scale bars, 10 μm.
951 Images are representative of four independent experiments. (**J**) Representative confocal images
952 of F-actin stained with phalloidin-488 in Calu-3 cells described in (H). Schematics with green lines
953 in the white dashed line boxes representing actin bundles, red cycles representing S-expressing
954 cells. White arrow heads in (I and J) indicate the enrichment or disappearance of F-actin, scale
955 bars, 10 μm. Images are representative of four independent experiments.

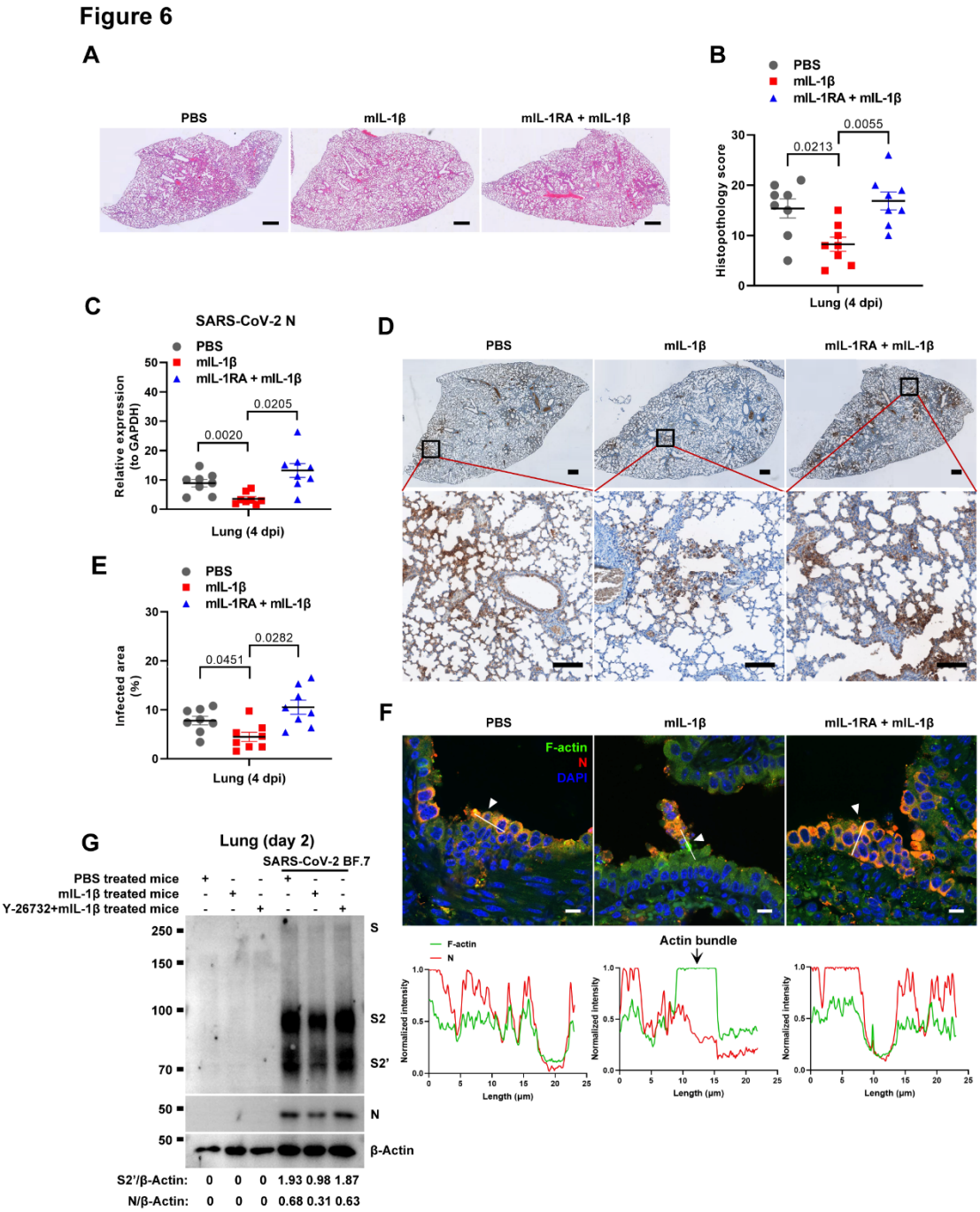

Fig. 6. IL-1β restricts SARS-CoV-2 transmission via induction of actin bundles in lung tissue.

(**A**) Schematic for a murine model of authentic SARS-CoV-2 infection, PBS control (n=8); 1 μg/kg mIL-1β (n=8); 150 μg/kg mIL-1RA + 1 μg/kg mIL-1β (n=8) were administered 1 hour before intranasal challenge with 5×10^4 FFU of SARS-CoV-2 B.1.351; mice were then intraperitoneal injection with PBS, mIL-1β and mIL-1RA + mIL-1β at 1 dpi and 2 dpi, before sacrificed at 4 dpi. (**B**) The body weights were assessed daily for weight loss after SARS-CoV-2 infection. (**C**) qPCR analysis of SARS-CoV-2 N mRNA collected from infected lung tissues at 4 dpi. (**D**)

965 Immunohistochemistry analysis of SARS-CoV-2 N staining in the lung tissue slices at 4 dpi, scale
966 bars are indicative of 500 μm (top panel), 50 μm (bottom panel) and images are representative of
967 eight independent experiments. (**E**) The percentages of SARS-CoV-2 infected area in (D) were
968 quantified. (**F**) Representative confocal images of F-actin stained with phalloidin-488 and SARS-
969 CoV-2 N in in the lung tissue slices at 4 dpi. White arrow heads indicate syncytia formation or
970 infected cells, scale bars are indicative of 10 μm and images are representative of three
971 independent experiments (Top). White lines indicate SARS-CoV-2 cell-cell transmission and
972 quantify with fluorescence intensity of F-actin and SARS-CoV-2 N (Bottom). (**G**) Immunoblots of
973 SARS-CoV-2 S, S2, cleaved S2' and N proteins collected from authentic SARS-CoV-2 BF.7
974 infected lung tissue cells, which isolated from BALB/c mice treated with PBS, 1 μg/kg mIL-1β or
975 1mg/kg Y-26732 + 1 μg/kg mIL-1β at day 2. Blots are representative of three individual
976 experiments. Numbers below the blots indicated the ratio of S2' or N versus β-Actin.